DOI:10.14753/SE.2023.2799

SEMMELWEIS EGYETEM

DOKTORI ISKOLA

Ph.D. értekezések

2799.

KISS BÁLINT

Celluláris és molekuláris biofizika
című program

Program- és témavezető: Dr. Kellermayer Miklós, egyetemi tanár

DOI:10.14753/SE.2023.2799

STRUCTURE, NANOMECHANICS AND INFECTION DYNAMICS OF SINGLE VIRUS PARTICLES

PhD thesis

Bálint Kiss

Doctoral School of Theoretical and Translational Medicine

Semmelweis University

Supervisor: Miklós Kellermayer, MD, D.Sc

Official reviewers: Péter Galajda, Ph.D
Orsolya Dobay, Ph.D

Head of the Complex Examination Committee: Alán Alpár, MD, D.Sc

Members of the Complex Examination Committee: László Cervenák, Ph.D
Mihály Kovács, D.Sc

Budapest
2022

DOI:10.14753/SE.2023.2799

Table of Contents

DOI:10.14753/SE.2023.2799

DOI:10.14753/SE.2023.2799

List of Abbreviations

Abbreviation	**Meaning**
AFM	atomic force microscopy
Alexa-NHS	alexa-488-N-hydroxysuccinimide
BSA	bovine serum albumin
BSL-3	biosafety level 3
COVID-19	coronavirus disease 2019
cryo-EM	cryogenic electron microscopy
Cypher ES	Cypher environmental scanner
DPSS	diode-pumped solid-state (laser)
EM-CCD	electron multiplying charge coupled device
GA	glutaraldehyde
LB	lysogeny broth
LPS	lipopolysaccharide
MOI	multiplicity of infection
PBS	phosphate buffered saline
PDMS	polydimethylsiloxane
PLL	poly-L-lysine
RBD	receptor-binding-domain
RNP	ribonucleoprotein
SARS-CoV-2	severe acute respiratory syndrome coronavirus 2
ssRNA	single-stranded ribonucleic acid
SyO	Sytox orange nucleic acid dye
TIRF	total internal reflection fluorescence
VP-SFM	virus production serum free medium

DOI:10.14753/SE.2023.2799

1. Introduction

While it is often debated whether viruses can be considered living organisms, in my view they are nature's "nanorobots" evolved to carry out a single function. Their main goal is to reprogram the host cell for viral reproduction. Viruses are comprised of a shell and a viral genome and can infect either eukaryotic or prokaryotic cells. Their infection cycle is closely intertwined with that of the host, and they can only reproduce through the complex process of infection. Their structure has evolved to achieve the most efficient genome delivery into their target, the mechanism of which can greatly vary among the different viral species.

Although nanoscopic in scale, viruses severely influence our macroscopic lives. Pandemics have been recurring throughout the history of mankind; however, in the past few years viruses had an even greater impact on the human population (1). The emergence of the recent global pandemic caused by the severe acute respiratory syndrome coronavirus 2 (SARS-CoV-2) has shifted the focus of many research groups towards this family of viruses (2, 3). Prior to the currently ongoing coronavirus disease 2019 (COVID-19) pandemic our research group has mostly focused on bacteriophage T7 (4-7). In my thesis, I will present our recent findings on the structure and infection cycle of both T7 and SARS-CoV-2 (8, 9).

SARS-CoV-2 is an enveloped single-stranded ribonucleic acid (ssRNA) virus with a corona-shaped layer of spike proteins, which play a crucial role in host recognition, and virus entry (Fig. 1) (10). Structural information about the spike protein has been acquired either on crystals of purified protein (11-14) or on fixed and frozen virus particles (15-17). It has been suggested that the spike hinges provide structural flexibility, which might increase host-recognition efficiency (15, 16). High-resolution cryogenic electron microscopy (cryo-EM) observations indicate that the ribonucleoprotein (RNP) of SARS-CoV-2 is partitioned into spherical, basketlike structures (17). These small spherical structures composed of RNA and proteins fill the viral particle. However, the surface dynamics and mechanical properties of native virions remain to be understood.

DOI:10.14753/SE.2023.2799

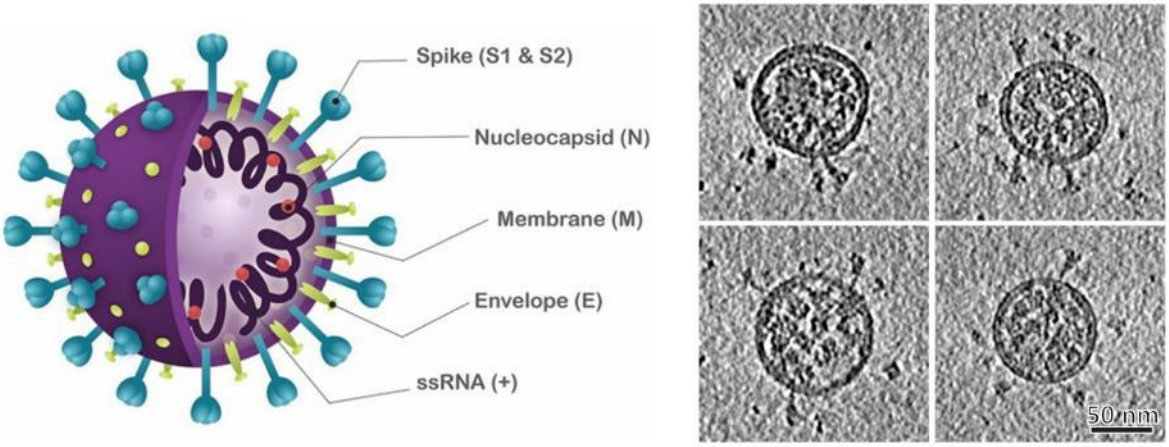

Fig. 1. ***Schematics and cryo-EM images of SARS-CoV-2.*** *Schematics of a SARS-CoV-2 particle (left), and four representative cryo-EM images of SARS-CoV-2 particles adapted from Ke et al. (right). (15, 18)*

Bacteriophages are regarded as a convenient model system, since working with them is not as hazardous as in the case of human pathogens. T7 bacteriophages are dsDNA viruses comprised of an icosahedral capsid with an internal protein core (which is unique to T7) and a short non-contractile tail (Fig. 2).

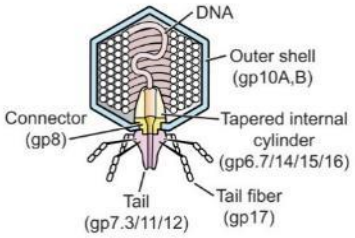

Fig. 2. ***Schematic structure of the T7 bacteriophage.*** *(19)*

This tail-fiber complex enables the phage to bind to its target and deliver its genome into the host (Fig. 3) (20). Although the structure and properties of T7 have been investigated extensively (5, 21, 22), our knowledge of its host-recognition and DNA injection mechanisms remain very incomplete (23, 24).

A recent cryo-EM study suggested that the tail-fiber complex might play a crucial role in docking and anchoring the bacteriophage to its target cell (25). The fibers were proposed to reversibly bind to either the capsid shell or the target cell surface and aid the search in finding the final target receptor. The search is thought to be terminated by the

DOI:10.14753/SE.2023.2799

binding of the tail to its receptor which then triggers the phage to eject its DNA. DNA is then translocated across the bacterial envelope into the target cell through an elongated channel assembled from the viral core proteins. Although the cryo-EM images provided details with unprecedented resolution, the dynamics of infection could only be indirectly inferred.

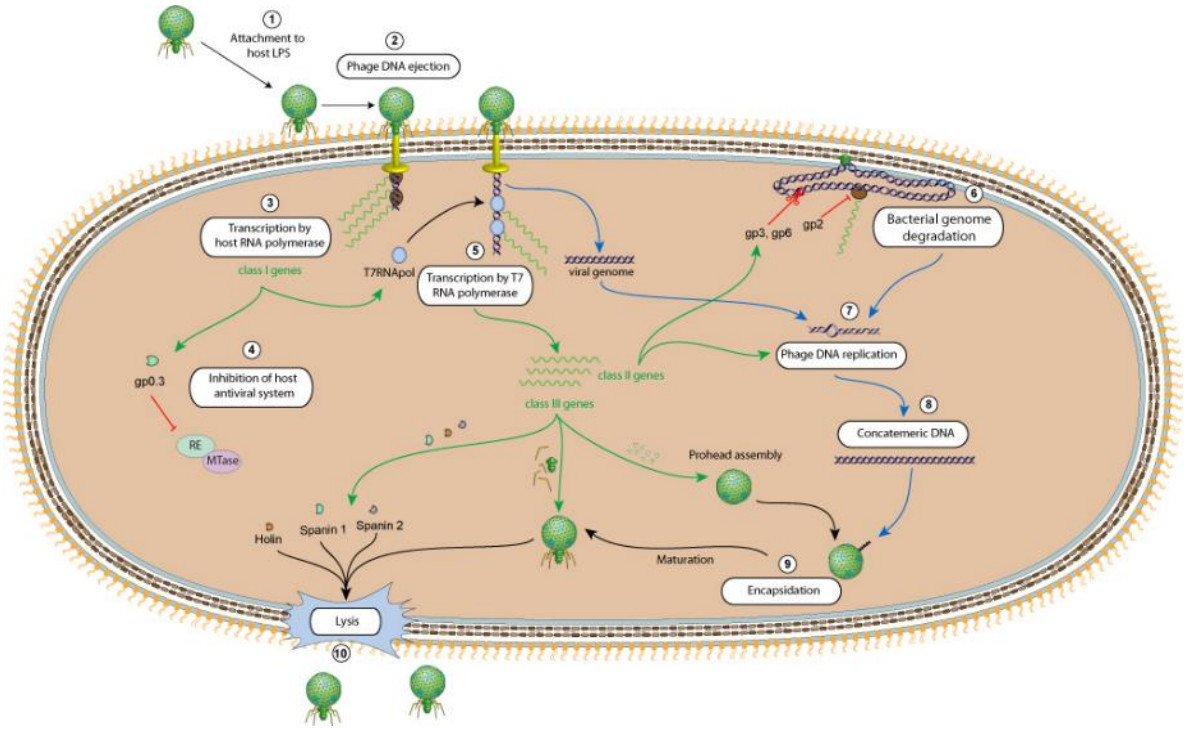

Fig. 3. ***Cycle of T7 infection.*** *(19)*

The driving forces and mechanisms utilized in the initial part of DNA injection have long been debated. Ejection is thought to be driven by the extreme pressure of DNA packed compactly inside the capsid, and/or by an active mechanism which would translocate the initial part of the genome through the host's membranes (24, 26). Further DNA translocation is first carried out by host proteins, then already expressed viral enzymes such as T7 RNA polymerases are thought to take over (23). *In vitro* DNA ejection studies have shown that viral genome release can be a strictly controlled, multistep process (27, 28). Such studies have not been performed with T7; however, in a unique approach, the DNA injection process of individual lambda phages was observed by fluorescently labeling the viral DNA (29). This work revealed a significant cell-to-cell variability in the kinetics of DNA translocation which would have remained hidden in bulk experiments. The experiment pointed out that the presence and healthiness of the

target cell cause high variability in the speed, hence timing, of DNA translocation (1-20 min to completion), compared with *in vitro* DNA ejection which was more uniform. In case of the lambda phage the genomic delivery might not be completely enzyme driven since the rate of DNA translocation decreases throughout the injection, dropping from ~20 kbp/min to zero. It has also been pointed out that the rate of DNA translocation in T7 appears to be more constant hence likely driven by enzymes (23). Although lambda is a long-tailed phage, similarities in DNA ejection to T7 can be expected.

Following successful genome translocation, viral replication is initiated, and new phages are formed. In the case of dsDNA bacteriophages, packaging the genome replicas into the freshly formed viral shells is a closely controlled and intricate process (30). The final stage of infection involves the release of the freshly assembled viral progeny. In case of T7, lysis is a multistep process, which involves pore formation in the inner membrane, followed by peptidoglycan digestion, and finally terminated by the local fusion of inner and outer membrane (31, 32). A recent study has shown that the bacterial envelope undergoes significant changes prior to lysis (33). Following viral infection, membrane blebbing and vesicle formation takes place, the role of which is yet to be determined.

In my thesis I will explain studies employing atomic force microscopy (AFM) and molecular force spectroscopy (22, 34, 35) which we used to investigate the topographical and nanomechanical properties of native SARS-CoV-2 virions, and to visualize individual host-cell bound T7 phages. Furthermore, fluorescence microscopy was utilized to visualize the target binding and DNA ejection process of T7 phages.

DOI:10.14753/SE.2023.2799

2. **Objectives**

Our long-term goal is to better understand viral structure which is closely related to the nanomechanical processes that control infection. Viral infection can be separated into three phases: target recognition, viral reproduction and finally the release of viral progeny. We aim to understand the first and final phases of infection by fluorescent labeling and AFM scanning, thereby observing the process of host recognition, docking and DNA release.

Our detailed goals and focuses are the following:

- Understanding the global structure and nanomechanics of SARS-CoV-2 virions.
- Investigating SARS-CoV-2 thermal stability.
- Understanding the target recognition and docking process of T7 bacteriophages.
- Uncovering the exact mechanisms of T7 DNA ejection.
- Exploring infection-induced global structural changes and lysis of the target bacterium.

3. Methods

The methods section has been adapted with slight modifications from two thesis-related publications (8, 9).

3.1 SARS-CoV-2 sample preparation

3.1.1 Purification of SARS-CoV-2

SARS-CoV-2 was isolated from the oropharyngeal swab of laboratory-confirmed COVID-19 patients in Hungary (Wuhan-Hu-1/2020) and passaged two times on VeroE6 cell lines (European Collection of Authenticated Cell Culture) in Dulbecco′s Modified Eagle′s - Medium (Lonza) supplemented with 5% fetal bovine serum (EuroClone) and Cell Culture Guard (PanReac AppliChem). To remove the disturbing effects of fetal bovine serum albumin (BSA), additional passage was carried out in virus production-serum free medium (VP-SFM), ultra-low protein medium (Gibco) supplemented with L-glutamine (Merck). Four days after inoculation, full cytopathic effects were observed, and the virus-containing medium was collected and centrifuged (3000 x g) to remove debris. To concentrate the virus, the supernatant was ultracentrifuged (70000 x g, 1.5 hours at 4 °C) in 8 x 13.5 ml lockable plastic tubes with a Sorvall MTX-150 ultracentrifuge. The supernatant was removed, and the pellet was resuspended in 100 µl VP-SFM tube. All sample preparation steps were performed in biosafety level-3 (BSL-3) conditions.

3.1.2 SARS-CoV-2 affinity surface binding via anti-spike antibody

100 µl of 0.1% w/v Poly-L-Lysine (PLL) (Merck) solution was dropped on freshly cleaved mica surface (Ted Pella) and incubated for 20 minutes, following which the surface was repeatedly rinsed with distilled water (purified with a Milli-Q Integral 3 Water Production Unit (Merck Millipore) and dried in N_2 stream (Linde Gáz Magyarország Zrt.). Incubation throughout the methods section was at room temperature, unless otherwise stated. 100 µl of 25% w/v grade I glutaraldehyde (GA) (Merck) was incubated on PLL surfaces for 30 min, followed by repeated rinsing with distilled water, then dried in N_2 stream. On this PLL-GA surface 100 µl of 10 µg/ml recombinant protein G (Merck) was incubated for 30 minutes, then washed repeatedly with 100 µl of phosphate buffered saline (PBS) (Merck). The last wash was replaced with 100 µl of 10

µg/ml SARS-CoV-2 Spike Glycoprotein Antibody (#abx376478, Abbexa), which was left on the surface for 1 hour. All surface functionalization steps were performed at room temperature. After washing off the unbound antibodies with repeated PBS rinsing, anti-spike glycoprotein (anti-spike) surfaces were stored under PBS for up to 5 days at 4 °C.

3.1.3 **Preparation of SARS-CoV-2 samples for AFM**

An aliquot (20 µl) of purified SARS-CoV-2 sample was pipetted onto the anti-spike antibody-coated substrate surface and incubated at 37 ˚C for 30 minutes, following which the surfaces were repeatedly washed with PBS. To increase virion surface density, another aliquot was added and incubated. The process was repeated twice. Subsequently, the surface was rinsed gently with PBS to remove unbound virions. All the sample-loading and washing steps were carried out in a laminar-flow hood in BSL-3 conditions (at the National Biosafety Laboratory, National Public Health Center, Hungary). Chemically inactivated SARS-CoV-2 samples intended for AFM imaging were prepared by pipetting 100 µl of 5% GA solution (in PBS) onto the sample, which was then incubated for >1 hour, ensuring both fixation and virus inactivation. Then, the sample was carried to the AFM laboratory (Department of Biophysics and Radiation Biology, Semmelweis University) for loading in the environmental scanner unit of the Cypher environmental scanner (Cypher ES) AFM instrument (Oxford Instruments). For imaging native virions, the fixation step was omitted, and the native sample was loaded directly into the Cypher ES Scanner. To ensure compliance with safety measures, a closed cantilever holder and gas-tight sample chamber was used, and the sample was loaded into the scanner in a laminar-flow hood in BSL-3 conditions. Then, the scanner was carried to the AFM laboratory and inserted into the AFM instrument for imaging. To further comply with safety measures, following AFM imaging the native virus samples were discarded in either of two ways. In the first, the AFM scanner was taken to the BSL-3 laboratory for removal and chemical destruction of the sample. In the second, the sample was heated to 90 ˚C for >10 minutes with the temperature-controller unit of the Cypher ES scanner. Then, the sample was removed for immediate chemical destruction (5% NaClO, Merck).

3.2 T7 and *E. coli* sample preparation

3.2.1 Bacterial cell growth and purification

E. coli (ATCC 11303) bacterial cell cultures were grown in lysogeny broth (LB) at 37 °C until OD_{550} of 1.0. OD_{550} value was determined by the measured absorbance of the undiluted bacterial culture at 550 nm wavelength with a Unicam UV4 spectrophotometer. Subsequently, the cells were collected by centrifugation. The pelleted cells were resuspended in PBS buffer, and centrifugation was repeated three times to exchange the growth medium to a more suitable buffer for proper immobilization of bacteria on PLL-coated mica and coverslip surface.

3.2.2 Surface preparation and modifications for phase-contrast imaging of T7-infected E. coli cells

Coverslips were cleaned by 10-min sonication in acetone (50 W, 1 s ON, 1 s OFF) in a bath sonicator (Techpan, TYPE UM-2), rinsing with purified water, and drying in vacuum. Mica sheets were freshly cleaved by using a piece of adhesive tape. 100 µl of PLL was dropped on either mica (for AFM measurements) or pre-cleaned coverslips (for TIRF, and phase-contrast microscopy imaging), incubated for 20 minutes at room temperature, washed with purified water, then dried in N_2 gas stream.

3.2.3 Bacterial cell immobilization

100 µl of *E. coli* cells diluted in PBS to OD_{550} of 0.1 were dropped on PLL-coated mica or coverslips, then the cells were allowed to adhere to the surface for 10 min at room temperature. Subsequently, the surface was repeatedly washed with LB (Merck) to remove unbound bacteria. T7 bacteriophages were added to LB in a 50:1 ratio relative to the number of bacterial cells. Purified T7 bacteriophages were a kind gift from the group of Gabriella Csík (36). Exchanging the buffer to LB and incubation at 37 °C was necessary for re-initiating bacterial growth while also enhancing viral host recognition. Upon changing the medium to PBS, bacteriophages still adhered to, and even lysed, bacteria; however, the process was much slower and less reliable, thus all experiments which involved live observation of T7 host recognition were performed in LB.

3.2.4 Sample fixation for high-resolution AFM imaging of T7 infected E. coli cells

The infection process was fixed at certain time points during the infection and imaged with AFM. Unbound bacteriophages were removed by first washing the infected, surface-immobilized cells with PBS. Bacterial immobilization and phage-to-host adhesion was stabilized, by 30 min incubation in 5 % GA/PBS solution, which was followed once again by repeatedly washing the surface with PBS.

3.2.5 TIRF microscopy of T7 infection of E. coli cells

Bacteriophage host recognition and DNA injection was observed by using a 100X oil immersion, total internal reflection fluorescence (TIRF) objective (Numerical aperture 1.49) in an Olympus IX81 inverted microscope. Fluorescence images were captured at various frame rates with an Andor iXon EM+ 885 electron multiplying charge coupled device (EM-CCD) camera with 512x512 pixel resolution. Imaging was performed with low-intensity phase-contrast illumination so that the unlabeled bacterial outline was apparent. 561 nm laser excitation was provided by an Omicron LightHUB Diode-Pumped Solid-State (DPSS) laser. T7 bacteriophages were labeled one hour prior to experiments via their internal DNA by Sytox Orange (SyO) at a final concentration of 1 µM. This intercalator dye was chosen due to its proven success in labeling viral DNA without disturbing DNA translocation and inhibition of DNA-dependent enzyme functions (29, 37). SyO has initially been used to label dead cells, since it does not cross the intact membrane of a living cell. Recorded image series were analyzed with Fiji, ImageJ software. Time stamps in the top right corner of videos and image series show the time passed since the moment of initial phage addition, unless stated otherwise. This initial time point is referred to as the start of infection.

3.2.6 Fluorescent labeling of T7 bacteriophages

For capsid behavior experiments, 10 µl of concentrated T7 phage solution was mixed with Alexa-488-N-hydroxysuccinimide (Alexa-NHS) (Thermo Fisher) to a final concentration of 1 mM, diluted in PBS, and allowed to incubate overnight at 4 °C in a rotorack. This treatment resulted in a non-specific labeling of the viral proteins. A 488

nm laser line was used to excite the fluorescent labeling to follow the position of viral proteins.

3.2.7 Single-phage T7 DNA-ejection experiments

To investigate the behavior of individual bacteriophages, an in-house polydimethylsiloxane (PDMS) microfluidic flow cell was designed and mounted on a coverslip bottom (Fig. 4A). The microfluidic channels used to observe the phages were 50 µm wide and 20 µm high. The above-mentioned TIRF experimental setup was used to observe the phages in this flow cell in a controlled flow environment (Fig. 4B). After flushing the flow cell with PBS, bacteriophages were injected and incubated to allow for surface adhesion. Bacteriophages were diluted to a concentration at which only a few phages were visible within a single frame. This dilution was necessary to prevent the overlapping of ejected DNAs. Following phage adhesion, the remaining phages were flushed out with PBS. Imaging was performed in 100 nM SyO at typical flow rates of ~1 mm/s.

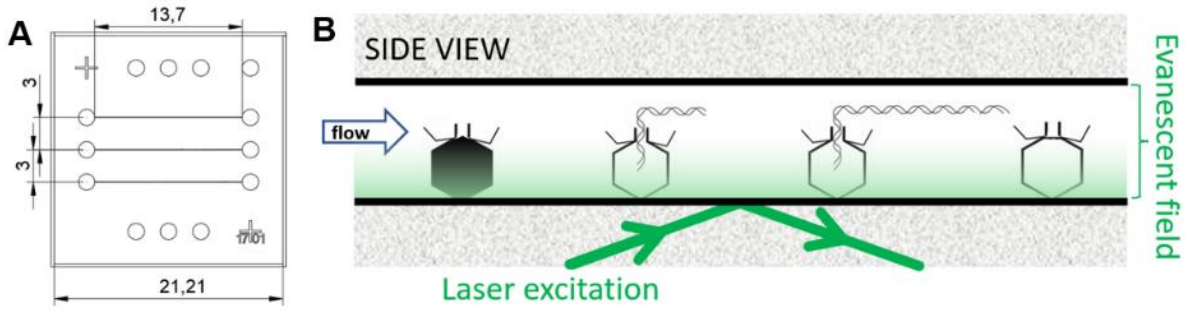

Fig. 4. ***TIRF experimental setup****.* ***(A)*** *Schematics of the PDMS microfluidic device. (B) T7 bacteriophages immobilized on the bottom surface of the microfluidic chamber*

3.2.8 Two-dimensionally restricted bead movement experiments

1 µl of fluorescent bead solution (Fluoresbrite carboxy microspheres NYO, d = 59 nm) was dropped on a coverslip, then a second coverslip was put on top of the bottom one. By tightly compressing the two coverslips a narrow chamber was formed, wherein the movement of the beads was restricted to quasi two dimensions.

3.2.9 **T7 target searching image analysis**

Image sequences of TIRF microscopy experiments were analyzed using the TrackMate ImageJ plugin (38). Particles of 0.5 µm apparent diameter were tracked throughout the recordings, their X-Y positions were collected and analyzed using TrackMate and Origin (OriginLab). Membrane roughness (Rq) was calculated on curvature corrected 1x1 µm regions of bacterial surfaces.

3.2.10 **Phase-contrast imaging of T7 infected E. coli cells**

Bacterial cell growth and lysis were observed at 100x magnification by using a Nikon Eclipse Ti inverted microscope. Image series were recorded at 5 s intervals with a Jenoptik Gryphax ProgRes camera with a resolution of 1920x1080 pixels.

3.3 **General description of AFM methods and image analysis**

3.3.1 **AFM imaging and force spectroscopy**

AFM imaging was carried out with an Asylum Research Cypher ES instrument. Scanning was performed in liquid at 20 °C either in PBS (SARS-CoV-2 and T7 samples) or in LB (T7 infection of *E. coli* cells), in non-contact mode with BL-AC40TS (Olympus) cantilevers (Fig. 5). Cantilevers were oscillated by BlueDrive technology (photothermal excitation) at an average free amplitude of 0.5 V, 350 mV setpoint, near the resonance frequency of the cantilevers, usually around 20 kHz. Images were acquired with a typical scanning speed of ~1 µm/s except for whole-cell *E. coli* scans, where the scanning speed was 5 µm/s. Force spectroscopy was carried out on targeted virions in contact mode, by lowering the cantilever with 0.5 µm/s velocity until the typical set force of 2 nN was reached. Cantilever spring constant was determined by the Sader method prior to imaging. Spring constant of BL-AC40TS cantilevers varied between 90-120 pN/nm. Compression experiments were carried out with PL2-CONTR-10 plateau probes (900 nm plateau tip radius, Nanosensors), which had a nominal spring constant of 280 pN/nm (Fig. 5). Image post-processing and analysis were performed by using the AFM driving software (IgorPro, WaveMetrics).

DOI:10.14753/SE.2023.2799

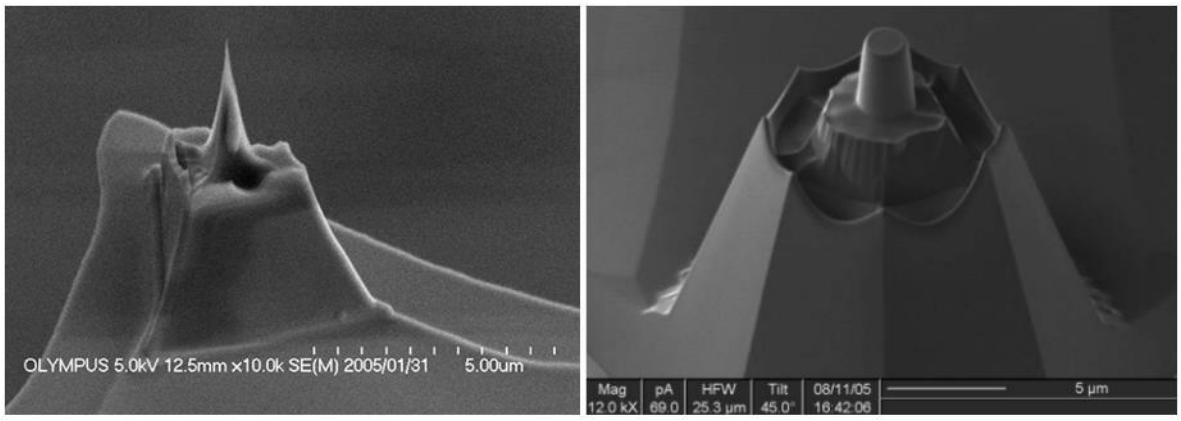

Fig. 5. ***Scanning electron microscopy images of BL-AC40TS (left) and PL2-CONTR (right) probe tips.*** *(Source of images: https://estore.oxinst.com)*

3.3.2 AFM image analysis and force curve analysis

Height, volume, diameter and distance measurements and the resulting statistics were calculated using the built-in functions of the AFM driving software.

3.3.3 Data analysis of SARS-CoV-2 sample topographies and force spectroscopy measurements

Image post-processing and data analysis were performed by using the AFM driving software AR16, IgorPro 6.37 (Wavemetrics). Particle analysis was carried out in subsequent analytical steps. First, the particles were demarcated by masking at the full width at half-maximal height. Second, the mask was eroded, then dilated to gently smooth particle edges, while also getting rid of small scanning artefacts. We ignored particles with obvious extreme deformities, ones too close to each other and with occupied areas smaller than 3000 nm^2. Topographical height was calculated in the centroid of the particles instead of using the maximal height value within the mask. Volume was calculated by the summation of the

height values of every pixel of the particle. Pixel area was dependent on image resolution. Diameter was calculated as the diameter of a circle with an area identical to that of the particles.

DOI:10.14753/SE.2023.2799

4. Results

4.1 SARS-CoV-2

Our recent publication describes the structure, nanomechanical properties and thermal stability of SARS-CoV-2 (9). These results are presented in detail throughout the following as well as the related discussion sections of my thesis.

4.1.1 Structure of fixed SARS-CoV-2 particles

The structure and topographical surface of SARS-CoV-2 particles was revealed by AFM. Viral particle immobilization was facilitated by antibody-enhanced affinity binding onto the surface. Antibody-mediated binding was necessary to increase the number of surface-adhered particles, as well as to increase the specificity of surface binding, thereby increasing the purity of the sample to be scanned (Fig. 6A).

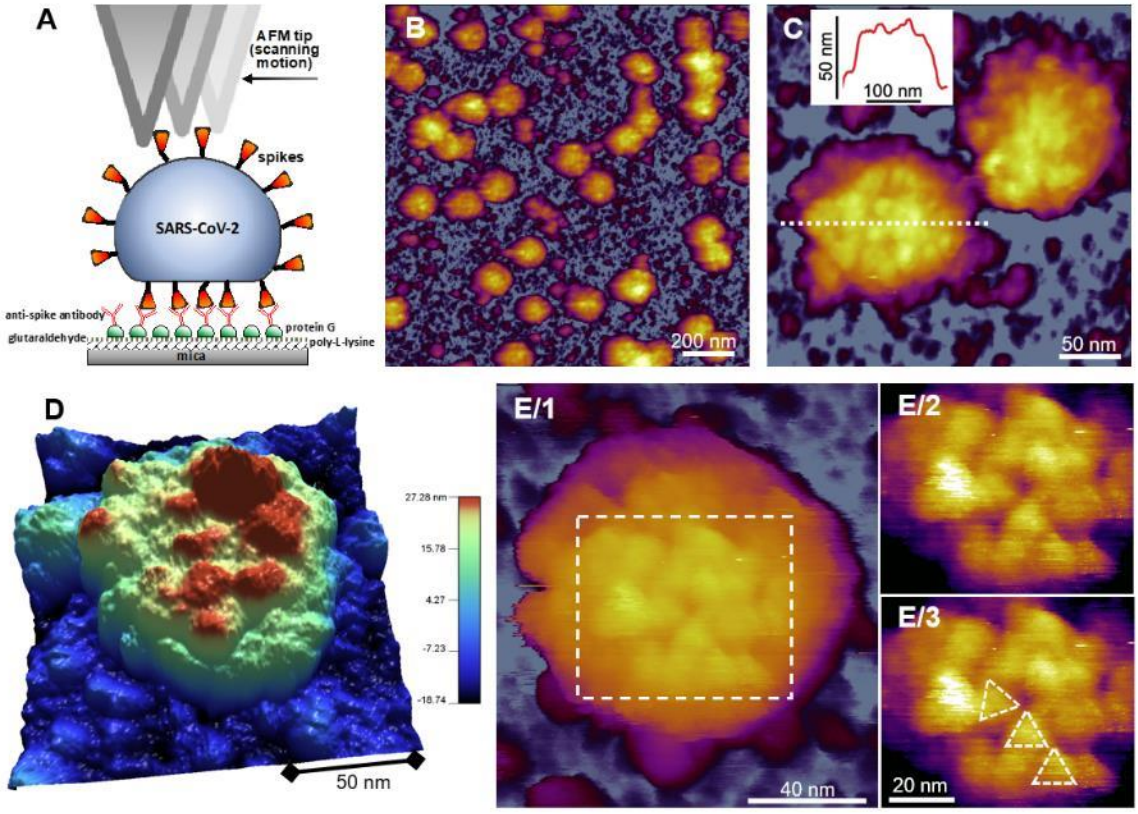

Fig. 6. ***Topographical structure of SARS-CoV-2 virions treated with 5 % glutaraldehyde for structural preservation****. **(A)** Schematics of scanning substrate-surface-bound virions with the AFM tip. **(B)** AFM image of an overview (1.5 x 1.5 µm) sample area. **(C)** Zoomed-in AFM image of SARS-CoV-2 virions. The virion surfaces are covered with protrusions that correspond to spikes (S protein trimers). **Inset**, topographical profile plot measured along the center of one of the virions (dotted line).*

The profile plot reveals a rugged surface. ***(D)*** *3D-rendered image of a SARS-CoV-2 virion. A somewhat flattened virion is observed, pointing at the global flexibility of the virion.* ***(E)*** *High-resolution AFM image of a SARS-CoV-2 virion displaying axial view of S trimers.* ***E/1*** *AFM image of the entire virion.* ***E/2*** *Enlarged and contrast-enhanced image of the rectangular area.* ***E/3****. The same AFM image with overlaid triangles indicating S trimer orientation. The spikes apparently display translational, rotational, and flexural disorder owing to their flexibility. (9)*

Affinity-enhanced surfaces increased the number of SARS-CoV-2 particles hundred-fold. Chemical fixation by glutaraldehyde was necessary due to safety reasons as well as to increase the strength of surface binding, thereby improving topographical resolution. Analysis of surface-bound particles had variable heights and diameters (62 ± 8 nm) (Table 1).

Table 1. Particle analysis results. Particle height was measured at the center of particles. We used the mean height of the native virion (d_v) to calculate its mean surface area (A_v) as $d_v^2\pi = 21642\ nm^2$. (9)

	Height ± S.D. (nm)	Volume ± S.D. (nm^3)	Diameter ± S.D. (nm)	n
Fixed	62 ± 8	574 000 ± 212 000	120 ± 16	51
Native	83 ± 7	490 000 ± 107 000	99 ± 11 nm	47
Heated (90 ˚C)	82 ± 10	600 000 ± 152 000	108 ± 12	37

Upon closer inspection, individual particles displayed a rugged surface decorated with protrusions (Fig. 6C), which was also confirmed by the 3D representation of the scanned area (Fig. 6D). In high-resolution AFM images (0.5 nm) we identified individual protrusions to be spike trimers based on their shape and size (Fig. 6E). Analysis of these high-resolution scans revealed the positional, flexural and rotational flexibility of the spike trimers (Fig. 7).

DOI:10.14753/SE.2023.2799

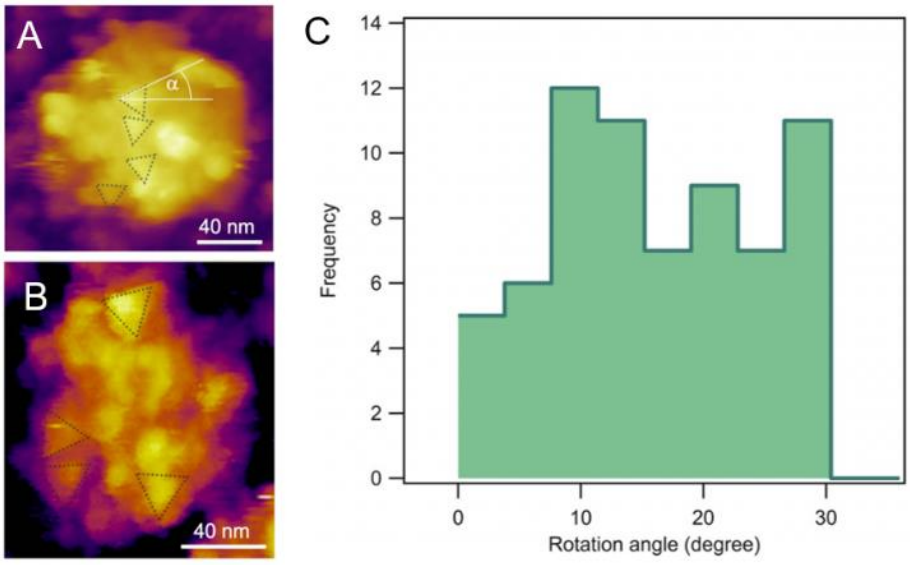

Fig. 7. ***Rotational flexibility of spike trimers****. **(A)** Topographical image of a SARS-CoV-2 particle depicting the principle of angle measurement: The rotational flexibility of spike trimers was measured by the angle between a horizontal line and the side of the triangular spike trimer closest to horizontal orientation. **(B)** An additional example of rotated spike trimers. **(C)** Distribution of the angular rotation of spike trimers compared to a horizontal line. (9)*

The mean nearest-neighbor distance between the S trimers and their topographical height were 21 ± 6 nm and 13 ± 5 nm, respectively (Table 2). From the mean nearest-neighbor distance and the virion dimensions we calculated that an average 61 spikes cover the SARS-CoV-2 virus particle surface (Table 2).

DOI:10.14753/SE.2023.2799

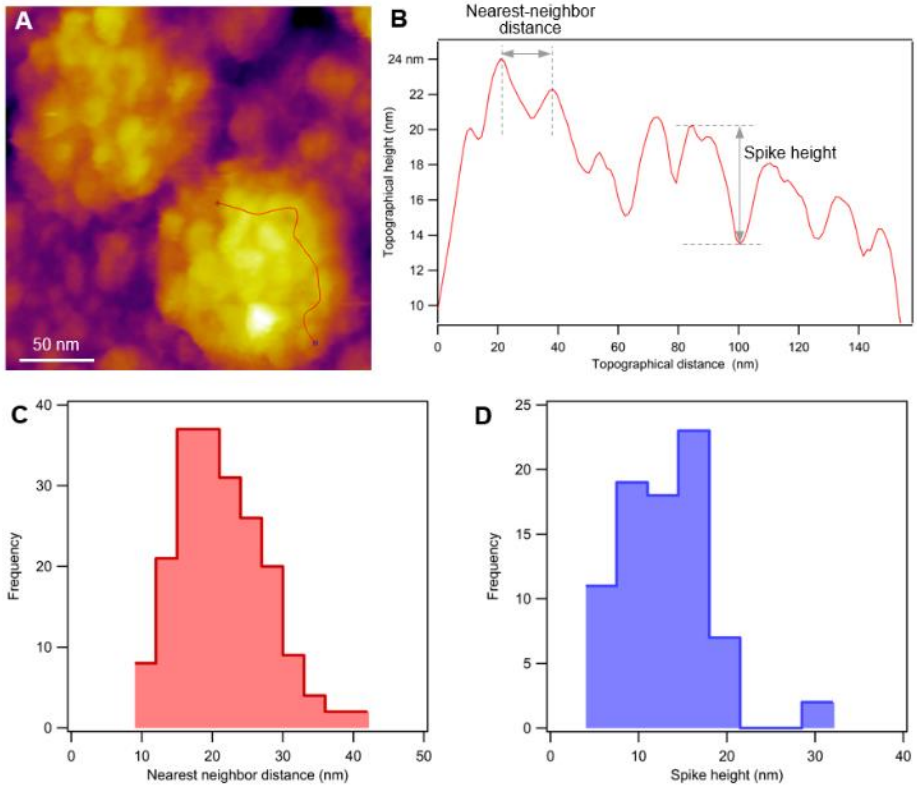

Fig. 8. ***Calculation of average spike height and nearest neighbor distance. (A)*** *Height-contrast image of two SARS-CoV-2 particles. Red line indicates the path, drawn approximately in coronal plane, along which the topographical height was measured.* ***(B)*** *Topographical profile plot of the virion along the line indicated in A. Nearest neighbor distance was obtained by measuring the distance between subsequent peaks. Spike height was obtained by measuring the distance, along the height axis, between a peak and the immediately following valley. Height was measured only for spikes with a large enough valley to increase the probability of the AFM tip reaching the envelope surface.* ***(C)*** *Distribution of the nearest neighbor distance between spikes (n=197), the wide range of which reflects positional disorder.* ***(D)*** *Distribution of the spike height (n=80), the wide range of which reflects flexural disorder. (9)*

Table 2. Spike analysis results. We assume that each spike occupies a circular area on the virion surface the diameter (d_s) of which is the mean nearest-neighbor distance. Hence, the mean area occupied by a spike is $(d_s/2)^2\pi = 356\ nm^2$. The ratio of the virion

and spike-occupancy surfaces provides the average number of spikes on a virion: ~61. (9)

	Mean ± S.D. (nm)	n
Nearest-neighbor distance	21 ± 6	197
Spike height	13 ± 5	80

4.1.2 Spike motion and structure of native SARS-CoV-2 particles

Chemical fixation can lead to the disruption of all biological samples; thus, their structure must be considered with caution. To circumvent this issue, and to compare the structure of native SARS-CoV-2 particles with those of the fixed ones, we have performed the AFM scanning of native, infective viruses (Fig. 9A). Scans revealed higher, more spherical viral particles (compared to the fixed ones) scattered on the surface. The particles had an average height of 83 ± 7 nm (Table 1) (Fig. 9B). The smooth surface and the increase in topographical height can be explained by an apparent dynamic surface caused by the rapid spike motion (Fig. 9C).

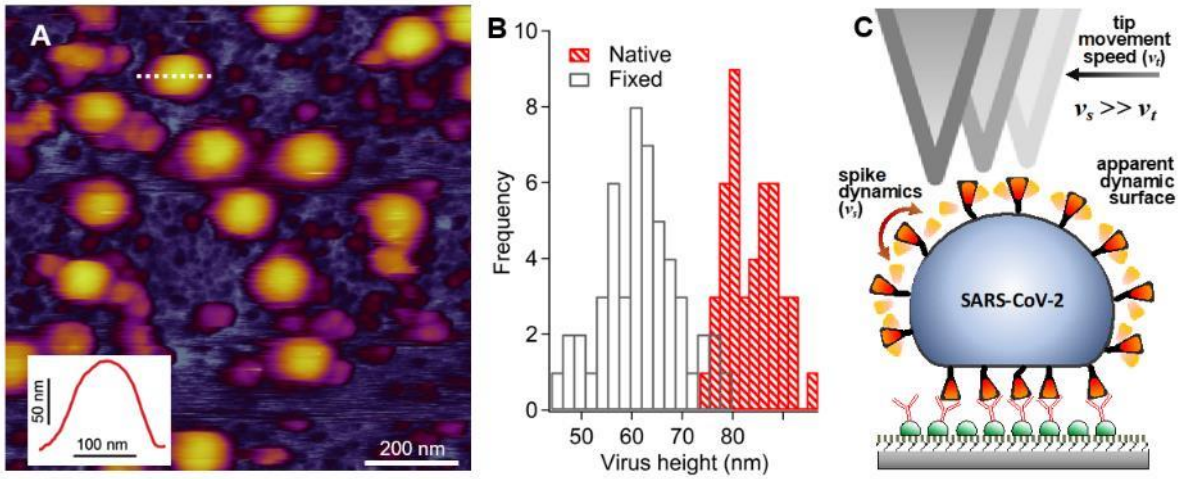

Fig. 9. ***Topographical analysis of native, unfixed SARS-CoV-2 virions. (A)*** *AFM image of an overview (1 x 1 µm) sample area. Surface protrusions are not resolved, and a blurred, smooth topography is observed.* ***Inset****, topographical profile plot measured along the center of one of the virions (dotted line). The profile plot reveals a smooth surface.* ***(B)*** *Distribution of the topographical maximal central height of fixed and unfixed SARS-CoV-2 virions obtained from particle analysis. Mean particle height (±S.D.) of fixed and unfixed virions are 62 ± 8 nm and 83 ± 7 nm, respectively. Unfixed virions have*

a significantly larger particle height than the fixed ones. ***(C)*** *Schematics explaining the dynamically increased height of the unfixed virion. (9)*

4.1.3 Nanomechanics of SARS-CoV-2

Apart from imaging, AFM can also be utilized to mechanically probe a sample, thereby providing unique structural and mechanical information. Following non-contact mode scanning (Fig. 10A), which allows the localization of individual viral particles, we have performed multiple nanomechanical indentation cycles on the viruses (Fig. 10B).

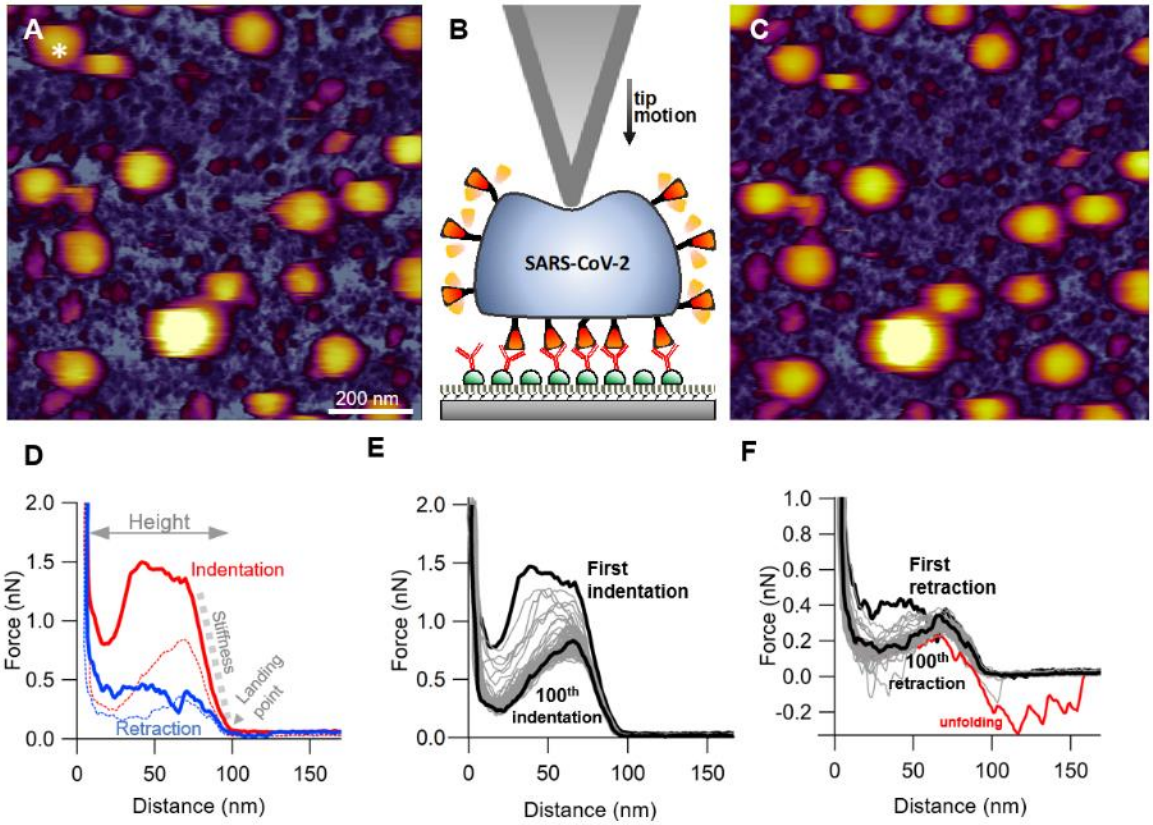

Fig. 10. ***Single-particle force spectroscopy of SARS-CoV-2 virions****.* ***(A)*** *AFM image of an overview (1 x 1 µm) sample area prior to nanomechanical manipulation. Asterisk shows a virion selected for nanomechanical manipulation.* ***(B)*** *Schematics of the force-spectroscopy experiment. The virion is indented with the AFM tip until a pre-set force (typically 2-3 nN) is reached.* ***(C)*** *AFM image of the same overview sample area following nanomechanical manipulation. We could not detect any topographical sign of permanent structural change.* ***(D)*** *Example of a force versus distance curve obtained during a single indentation-retraction cycle. From the slope of the indentation curve (gray dotted line) and the distance between the landing point and substrate limit of the trace we obtained*

the stiffness and the force-spectroscopic height of the virions, respectively. Red and blue dotted lines indicate indentation and retraction data, respectively, obtained in the 100th nanomechanical cycle. ***(E)*** *Force versus distance curves obtained during repeated indentation of a single SARS-CoV-2 virion.* ***(F)*** *The matching force versus distance curves obtained during retraction. In some traces force sawteeth (red trace) corresponding to the unfolding of surface proteins. (9)*

Virus indentation was performed with a constant velocity of 0.5 µm/s until a preset level of force was reached (typically 2-3 nN). The mean force-spectroscopical height was 94 ± 10 nm (n = 40), which is comparable to that obtained from topographical data. Remarkably, the virions could be compressed wall-to-wall. By surprise, the severe nanomechanical indentation did not result in visible topographical changes (Fig. 10C). The indentation cycle could be partitioned into multiple stages. Initially, landing on the virion is followed by an elastic compression phase, the steepness of which corresponds to the stiffness of the virions (Fig. 10D). The mean stiffness of the virions was 13 ± 5 pN/nm (n = 40). The linear compression region is then followed by a yield point at which the virion structure suddenly changes. From this point onward, internal force-induced structural transitions take place until total wall-to-wall compression occurs, after which the tip immediately hits the substrate surface. Following complete indentation and upon reaching the preset force limit the cantilever is retracted. Interestingly, the virion exerted forces on the cantilever on the magnitude of several hundreds of piconewtons during the retraction cycle, which means that internal rearrangement of the previously disrupted structure is taking place against force. Such forces were present until the height of the previously indented particle was reached. Indentation and retraction curves displayed hysteresis, indicating that part of the invested mechanical energy was dissipated as heat. Indentation cycles could be repeated up to 100 times. However, and to our surprise, apart from a slight fatigue, the virions never broke or collapsed (Fig. 10E). Indentation and retraction cycles relaxed after a couple dozens of cycles, then the hysteresis decreased. In a few retraction curves (~1%) protein unfolding, marked by force sawteeth with peak forces of ~250 pN took place (Fig. 10F).

The sharp AFM tip employed in the above experiments has the advantage of accurately localizing surface-adhered particles with nanometer scale accuracy, which can then be mechanically probed one-by-one with high precision. However, indentation of a virion

with a sharp tip can result in the membrane becoming pierced, or the virion might become dislocated due to weak surface adhesion. An alternative method is the use of so-called "plateau probes" which have a flat tip with a large surface (Fig. 11). Such a probe allows the mechanical manipulation of the virus as if it was squeezed between two flat plates.

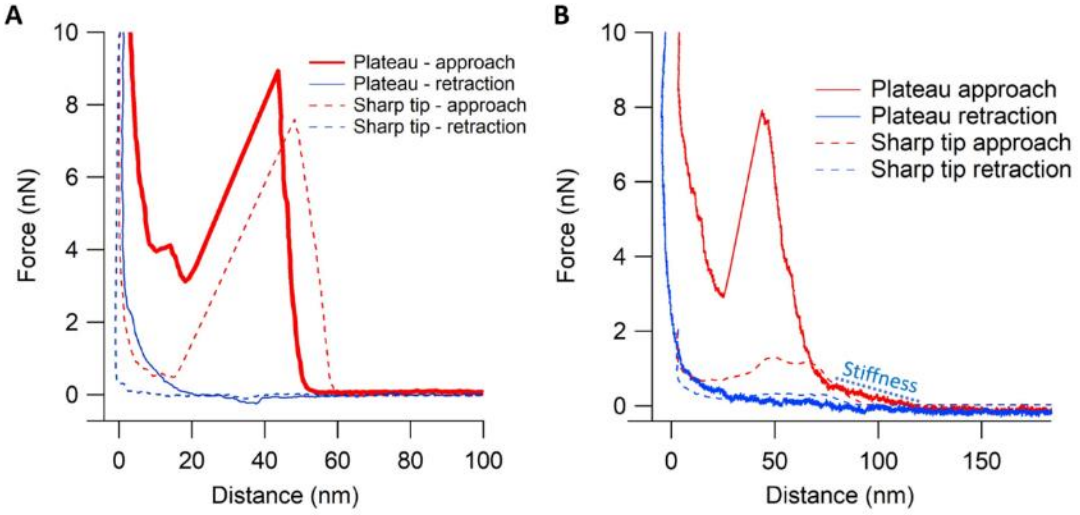

Fig. 11. ***Comparison of plateau vs. sharp tip compression.*** *Plateau and sharp tip compression of a T7 bacteriophage* ***(A)*** *and a SARS-CoV-2 particle* ***(B)****. (In review)*

To our knowledge, such probes have not yet been implemented in nanoindentation experiments on viruses. Although high-resolution scanning is not possible with a plateau probe, it can provide distinctive nanomechanical data compared to sharp tips. Nanoindentation experiments carried out with a plateau probe are in a sense similar to a mechanical press. If the planes of the substrate surface and the plateau are parallel to each other, indentation becomes more like a compression. Since localization is not possible, sample surfaces were saturated with viruses to an extent where every compression cycle was expected to compress at least one virion. Compression cycles of a single virion result in a different type of force-response when compared to regular sharp tip indentations. Sharp tip indentation and plateau probe compression can provide two different force-response datasets, thereby providing two independent methods of mechanical probing. In case of the rigid protein capsid of T7 indentation cycles by the two different probes provide similar datasets (Fig. 11A). SARS-CoV-2, being a less stiff virus, behaves in a different way depending on the type of tip used (Fig. 11B). In the initial region of indentation, similar stiffness can be measured as with the sharp tip, leading to a linear

increase in force. This region is followed by a yield point (higher than that of the sharp-tip yield point), leading to internal viral transitions. Sharp tip indentation cycles are repeatable as described in the previous section. By contrast, compression with the plateau tip leads to the irreversible deformation of the global viral structure.

4.1.4 Thermal sensitivity of SARS-CoV-2

To explore the thermal stability of SARS-CoV-2 viruses, we have performed heat treatment experiments and visualized their effects with AFM (Fig. 12). Surface-adhered virions were exposed to 60 (Fig. 12A), 80 (Fig. 12B) and 90 °C (Fig. 12C) for 10 minutes before cooling the sample back to 20 °C for post-heat-shock imaging. Virions remained on the surface, and their global appearance was only slightly altered. They appeared somewhat faceted, but they retained their blurry surfaces. To test whether the spikes were still present, we fixed the samples (5% GA) following 90 °C temperature treatment (Fig. 12DE). The rough surface seen in control samples was retained, but the number of spikes appeared to be smaller. Furthermore, their trigonal shape was less distinct, suggesting that partial thermal denaturation may have taken place. Virion surfaces were progressively denuded as the temperature was increased, suggesting that spikes might be gradually removed from the virion surface due to heating. As a result of heating the strength of virus to surface adhesion can be expected to decrease, however there was no apparent decrease in the number of surface adhered particles.

DOI:10.14753/SE.2023.2799

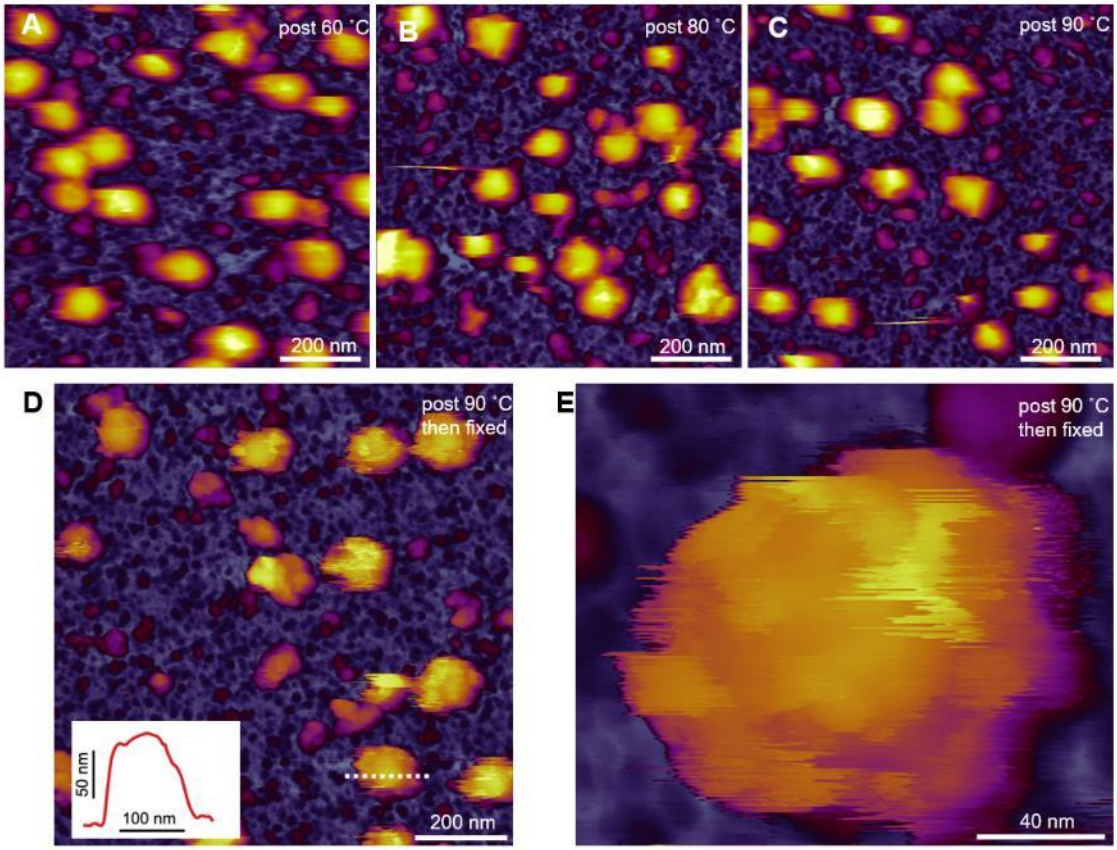

Fig. 12. ***Effect of temperature change on the topographical structure of SARS-CoV-2****. The sample was heated for ten minutes at 60 (**A**), 80 (**B**) and 90 ˚C **(C)**, then cooled back to 20 ˚C prior to AFM imaging. The virions persist on the substrate surface with their global structure nearly intact, but the topography becomes progressively more rugged, pointing at the gradual disappearance of the dynamic surface smoothing hence reduction of spike dynamics. (**D)** AFM image of an overview (1 x 1 µm) sample area following thermal treatment (90 ˚C for ten minutes) and glutaraldehyde (5%) fixation.* ***Inset****, topographical profile plot measured along the center of one of the virions (dotted line). The rugged surface topography is partially restored, but large areas on the virions are devoid of spikes.* ***(E).*** *High-resolution AFM image of a heat-exposed (90 ˚C for ten minutes) and fixed (5% glutaraldehyde) SARS-CoV-2 virion. Shallow surface protrusions are present. (9)*

4.2 T7 bacteriophage

Our recent publication summarizes our findings related to the infection cycle of the T7 bacteriophage on a single-phage level (8). These results are presented in detail throughout the following as well as in the related sections of the discussion.

AFM scans of T7 samples reveal icosahedral particles scattered on the substrate surface surrounded by DNA strands (Fig. 13A). Tail complexes and viral fibers are visible in high-resolution images of individual viruses (Fig. 13B). Contrary to popular belief, the viral fibers are lying on the capsid surface in a swastika-like orientation and conformation. The total length of viral fibers is 49 ± 6 nm.

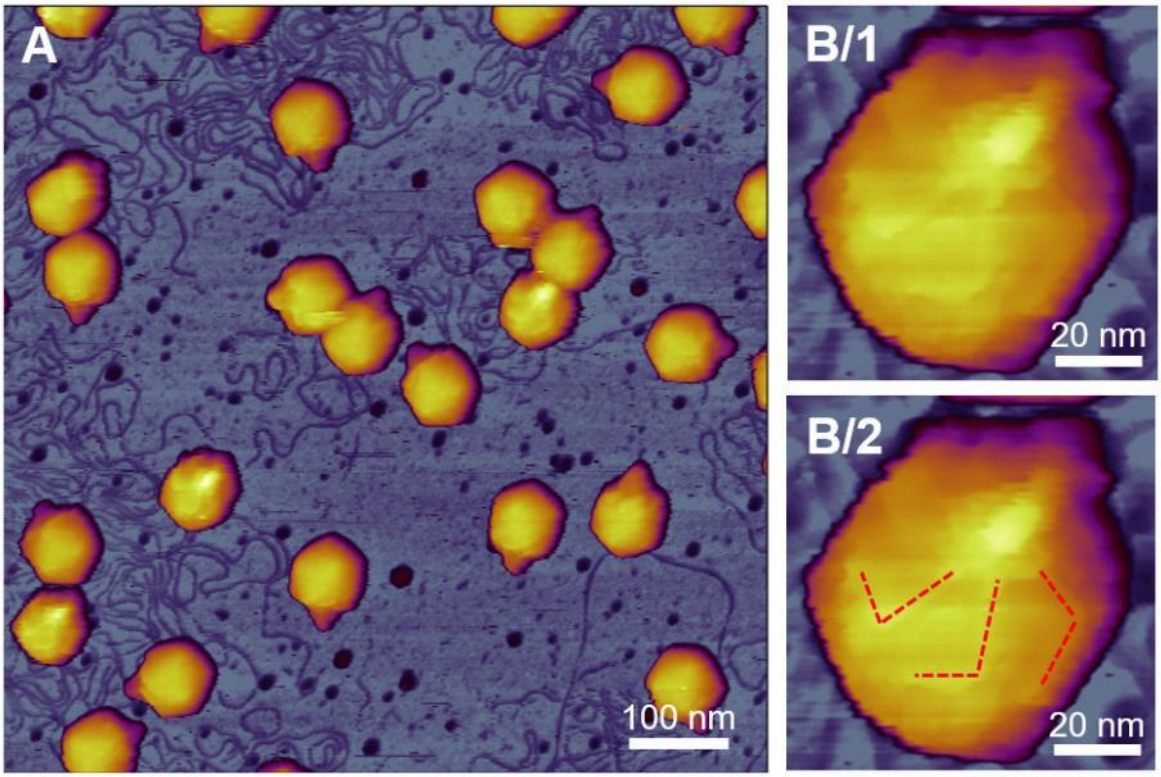

Fig. 13. ***AFM image of T7 bacteriophages.*** *Height-contrast image of bacteriophages and viral DNA* ***(A)****. Enlarged image of a single T7 bacteriophage* ***(B/1)*** *and the same image with the tail-fibers marked with red lines* ***(B/2)****.*

4.2.1 Buffer composition and further environmental factors influencing the T7 infection cycle

To optimize the environmental circumstances of the single-particle assays, we first quantitated the effects of culture media, phage-to-cell ratio (multiplicity of infection, MOI) and DNA-staining dye concentration on the growth rate of bacterial populations. If we used LB medium, which is optimal for bacterial growth, then lysis occurred after ~30 minutes in a synchronized manner. By contrast, in PBS, which is more suitable for TIRF as well as AFM measurements (due to its higher transparency) growth rate declined strongly, and a synchronized lysis could not be observed within 120 minutes (Fig. 14A). Even though bacteria were unable to multiply in PBS, they remained alive and accessible for infection. The phage-to-cell ratio also affects lysis dynamics (Fig. 14B) (39) due to the fine balance between the amount of accessible resources set by host metabolism and the demand set by the number of phages simultaneously infecting the cell. At low MOI (~1), bacterial growth proceeded slowly and was not interrupted (Fig. 14B gray trace). At very high MOI (~500), the bacterial population declined progressively due to overinfection, and a deterministic lysis needed for single-particle analysis was absent (Fig. 14B blue trace). At the intermediate MOI of 50, a synchronized, deterministic lysis could be observed after ~40 minutes (Fig. 14B red trace). Because the estimated ratio of infective to non-infective phages was as low as 1:5 (determined by viral titration), the true MOI was estimated to be about 10. In subsequent experiments, this adjusted MOI was used. Finally, we tested the effect of SyO on infection dynamics and observed that lysis was only slightly delayed and prolonged (Fig. 14C).

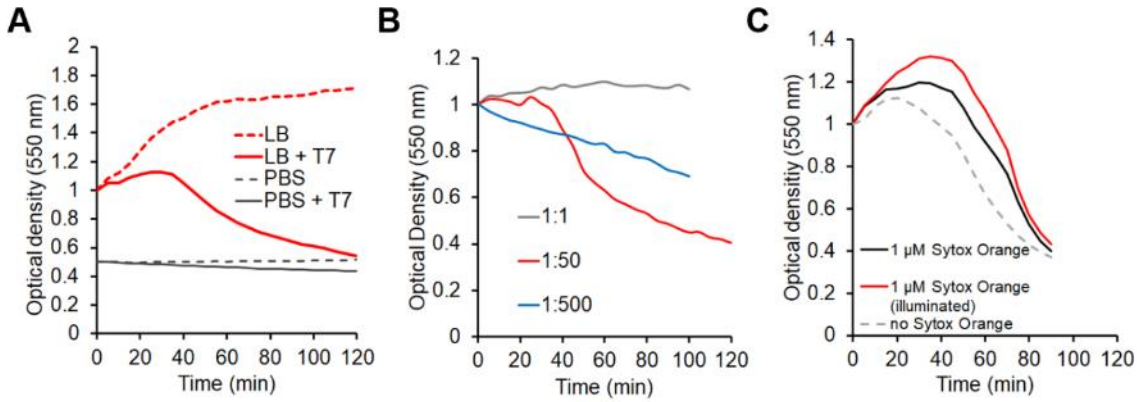

Fig. 14. ***Bacterial growth kinetics: (A)*** *Buffer composition influences bacterial growth.* ***(B)*** *Different MOIs have a significant impact on bacterial lysis.* ***(C)*** *Intercalator dyes delay and prolong infection induced bacterial lysis. Optical density measurements were carried out in LB unless otherwise stated. (8)*

4.2.2 T7 explores the *E. coli* surface for binding site

To follow the target recognition kinetics and DNA translocation process of bacteriophages, their DNA was labelled with SyO by allowing the dye to penetrate the capsid shell. Docked bacteriophages appeared as bright fluorescent particles along the edge of the bacterium (Fig. 15A). Phage binding to *E. coli* was isotropic, as we could not observe any directional or spatial preference. To reveal the surface dynamics of individual phage particles, we tracked the position of the fluorescent spots as a function of time. In the early stages of infection, bacteriophages that retained their genomes long enough to be observed for several minutes moved around randomly on the target cell surface (Fig. 15A, 2B). Although phage movement occasionally accelerated (Fig. 15A/2, C) and eventually stopped altogether (Fig. 15B), initial periods of random motion with a more-or-less constant velocity were well discernible. The displacement of the phage particles from their landing point as a function of time (Fig. 15C) could be fitted with a power function with fractional exponent, suggesting diffusive motion. At room temperature, the random target search proceeded for several minutes (Fig. 15CD). The total travel path grew linearly and could reach up to 5 µm (Fig. 15D). The mean slope of this function was ~10 nm/s. The step size of the motion, measured as the displacement of particle position between consecutive video frames spaced 1 s apart, was normally distributed with a mean of ~10 nm (Fig. 15E), suggesting that T7 particles search for their target site with an average speed of 10 nm/s. To test whether the target search is free diffusion, we measured,

with identical analytical tools, the two-dimensional diffusion of polystyrene beads with radii similar to that of T7's (Fig. 15E). Although the overall shape of the bead step-size distribution was similar to that of the T7 particles, notably, the mean step size was shifted to 5 µm, indicating that the average speed of bead motion was nearly two orders of magnitude greater than that of target search by T7. Thus, target search is a diffusive motion the speed of which is limited, most likely, by reversible interactions between the virus and the host cell surface.

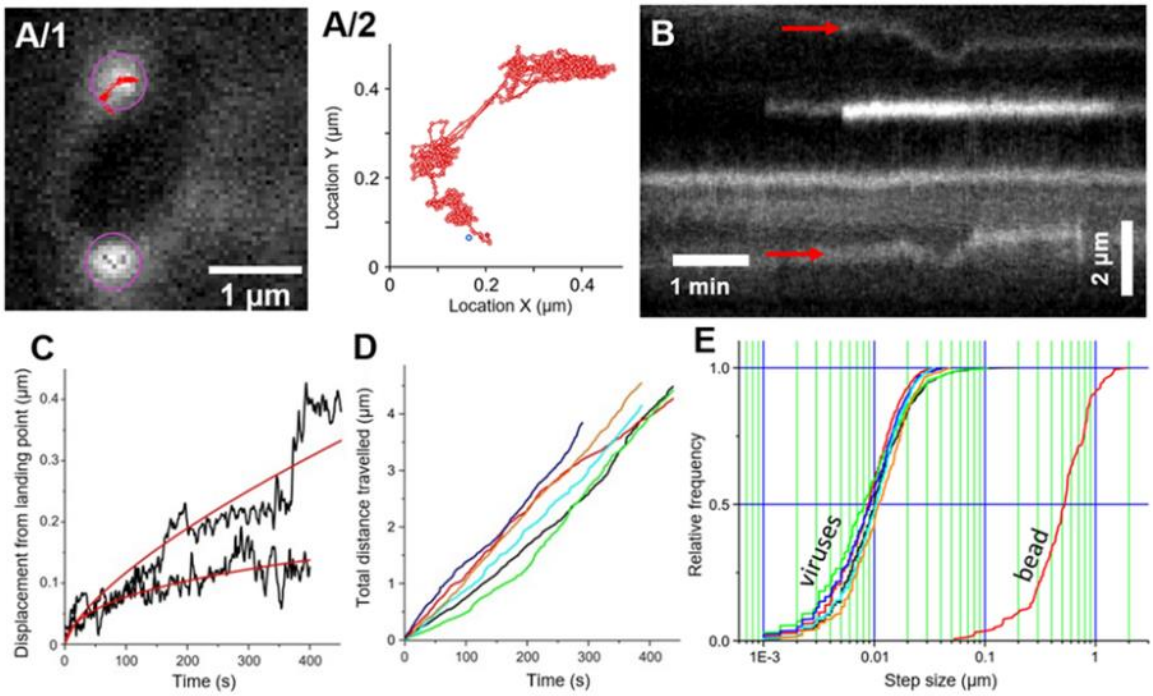

Fig. 15. ***Phages travel on the bacterial surface****. **(A)** Bacteriophages searching on the surface of a bacterium: **(A/1)** Purple circles show tracked particles, red line shows the trajectory of the upper particle. **(A/2)** Enlarged graph of the trajectory shown in A/1, blue spot shows the initial binding point. **(B)** Kymograph of bacteriophages travelling along the bacterial periphery. Red arrows show the initial docking position of two phages. **(C)** Black curves show the distance of two tracked viruses from their landing point over time, red line shows a parabolic function fitted to the data with exponents of 0.64 and 0.43. **(D)** Total distance traveled by tracked phages from their initial binding point. Different colors correspond to different viruses. **(E)** Cumulative step size distribution of bacteriophages, and a 60 nm diameter bead. When comparing the step size distributions of viruses and*

that of the bead, it must be noted that the movement of phages was recorded at 1 frame per second, while the movement of beads was recorded at 10 frames per second. (8)

4.2.3 The fate of the released viral genome

To reveal the fate of individual, docked phage particles and their genomic DNA, we constructed circumferential kymograms by plotting the intensity profile along the bacterium's edge as a function of time (Fig. 16AB). The fluorescence intensity of the T7 particles related to DNA labeling decreased as a function of time. Depending on the kinetics of the intensity drop we identified three different processes taken by the virus particles or their DNA. First, and most frequently, intensity decayed with an exponential process, which corresponds to the injection of viral DNA into the target cell (Fig. 16ABC, phage a). By analyzing the drop in the intensity of the fluorescent signal, we can hypothesize that 90% of the genome is injected after 1 min. Second, intensity sometimes dropped, but then it increased and fluctuated. This process corresponds to "misfiring" by the T7 phage, during which the genomic DNA is ejected into the surroundings rather than into the host cell (Fig. 16AB, phage b). Interestingly, misfiring became more frequent in the later stage of infection, and floating, partially ejected DNA strands could be seen around docked bacteriophages. Third, the fluorescence signal sometimes disappeared within a single frame, which corresponds to unbinding of the T7 phage particle from the host surface. The finding indicates that partial target binding of T7 is reversible. We note that rapid misfiring events were sometimes difficult to distinguish from quick unbinding events (Fig. 16A b and b* phages).

DOI:10.14753/SE.2023.2799

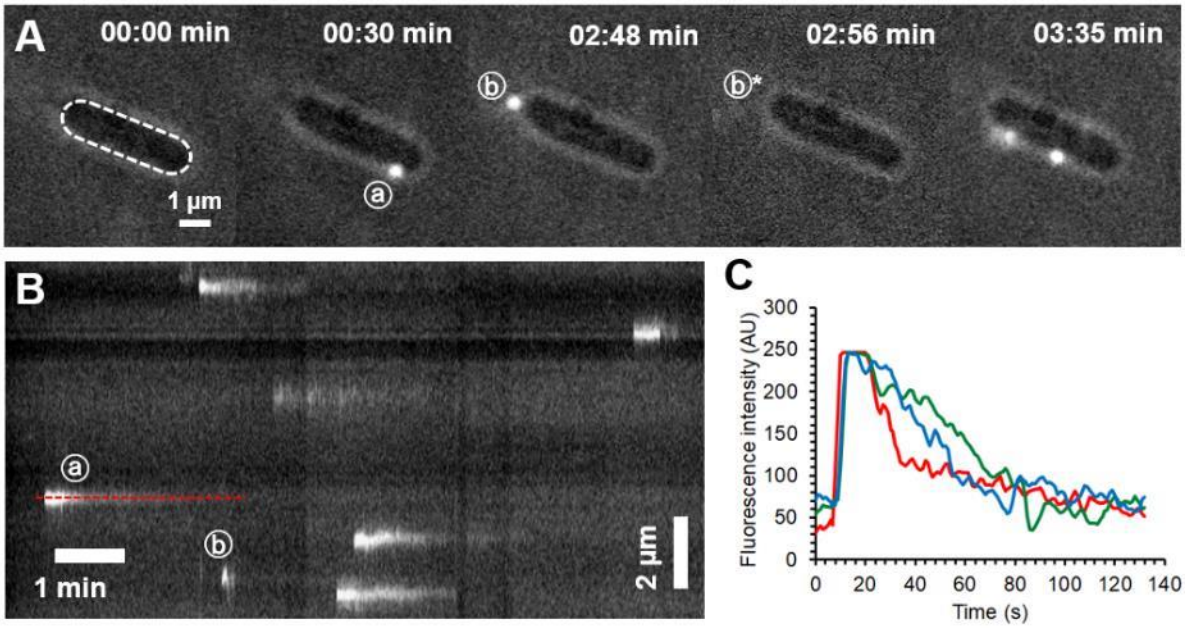

Fig. 16. ***Single-phage infection process. (A)*** *Snapshots of the early moments (0-10 min) of a single bacterium infection highlighting the docking of bacteriophages. Bacterial outline is slightly visible due to low levels of phase-contrast illumination. Dashed white line indicates the bacterial periphery along which a kymograph* ***(B)*** *was constructed. The same two phages are marked with circled a and b in the snapshots (A) and the kymograph (B). b* marks the position where phage b was visible 8 seconds earlier. Red dashed line marks the location of the relative intensity profile of a single phage (a) shown in red in* ***(C)****. The intensity profile of two additional phages are also shown with green blue. (8)*

4.2.4 Structural dynamics of the infected host cell surface

TIRF microscopy allowed the visualization of the docking process of bacteriophages with high temporal resolution, but it was only able to image the coverslip-facing side of immobilized bacteria, and only to a depth of ~200 nm. Considering that the circumferential diameter of an *E. coli* cell is about 800 nm (measured with AFM), cell surface events remain hidden. To reveal the topographical changes of the host cell caused by T7 infection, we scanned their surface with high-resolution AFM (Fig. 17). AFM, similarly to TIRF microscopy, revealed increasing number of docked phages, which were identified by their consistent 60 nm height (Fig. 17A). Viruses saturated the bacterial surface with time (~1 hour at room temperature). To achieve more stable imaging,

chemical fixatives were added to stabilize bacterium-to-surface as well as phage-to-bacterium adhesion. Snapshots revealed a surface covered by bacteria at different stages of infection, depending on the moment of fixation. Samples fixed after 15 minutes consisted of intact bacteria which had small bumps extending from their membrane surface (root-mean-square roughness, Rq = 5.2) (Fig. 17B). These extending bumps were identified by their height (~60 nm protrusions) and shape to be individual T7 bacteriophages (Fig. 17B, inset). Bacteriophages showed no site preference in docking, as they were distributed evenly throughout the bacterial surface. If infection was allowed to proceed for 30 minutes (Fig. 17C), then the number of successfully docked phages per bacteria increased to an average 10 phages per bacterium, which at this point matched our calculated starting ratio (MOI = 10) (Fig. 18). After 30 minutes the bacterial surface became rougher (Rq = 11.4), which was never observed in non-infected bacteria. After 45 minutes, lysis of individual bacteria started in a highly synchronized manner. The final stages of infection were captured on samples which were fixed after 60 minutes (Fig. 17D). At this point a large portion of the surface-bound bacteria have already lysed, and only their remnants were found. Many of the bacteria which were still intact, appeared morphologically very different from those seen at earlier stages. Their surface roughness increased further (Rq = 18.2), and membrane protrusions (blebs) started to appear. These blebs had a diameter of 246 $\pm$ 62 nm. Their formation can only be attributed to viral infection since they never appeared on the surface of non-infected bacteria. In some cases, bacteriophage-to-host connections were stable enough to allow high-resolution scanning, which revealed the nanoscale details of viral infection (Fig. 17D/1). In the 3D representation of these images, individual bacteriophages could be identified by their tail fibers attached to the host cell in a similar configuration seen in cryo-EM images (Fig. 17D/2) (25). The number of docked bacteriophages started to decrease after 45 minutes to an average six phages per bacterium, compared to the steady increase seen in TIRF images (Fig. 18). The apparent decline in phage number is most likely directly related to bleb formation that prevents the topographical detection of phage particles but allows for detection by fluorescence.

DOI:10.14753/SE.2023.2799

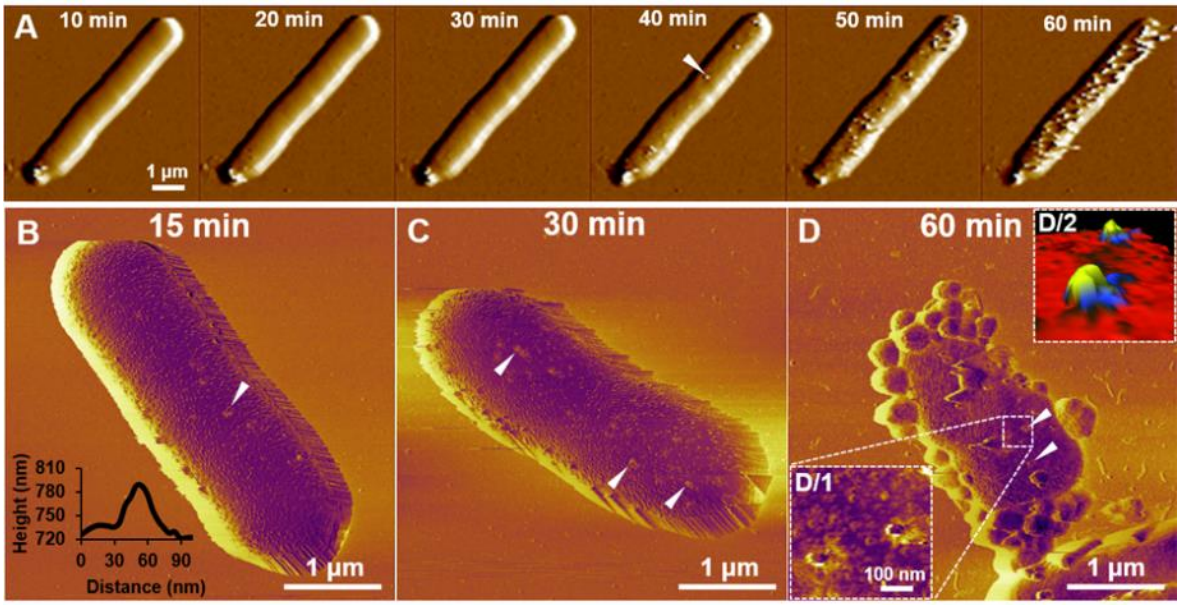

Fig. 17. ***Viral infection causes bacterial cell surface roughening and bleb formation.*** ***(A)*** *Amplitude-contrast image series of viruses docking on a single bacterial cell surface in native conditions at 25 °C. White arrowhead points to a docked bacteriophage. Phase-contrast AFM images of E. coli bacteria fixed with glutaraldehyde 15* ***(B)****, 30* ***(C)*** *and 60* ***(D)*** *minutes post-infection. Inset in B shows the height section profile of the host cell bound phage indicated by a white arrowhead. 60 minutes after infection bleb formation can be observed. White arrowheads point to docked bacteriophages. Insets show the enlarged region of two docked bacteriophages* ***(D/1)*** *and their 3D representations* ***(D/2)****, yellow and blue color shows the viral capsids and black color shows the surface bound tail fibers. (8)*

DOI:10.14753/SE.2023.2799

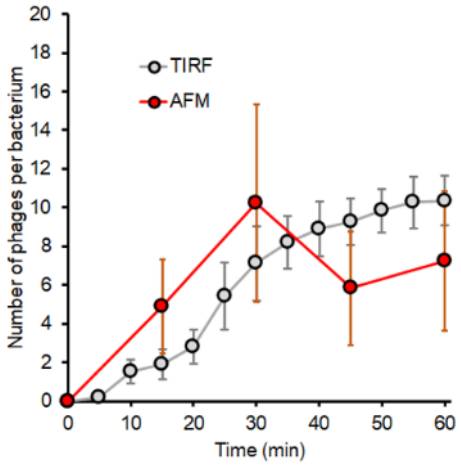

Fig. 18. ***Bacteriophages bind to the bacterial surface over-time****. The number of docked bacteriophages followed by TIRF and AFM. N=24 for TIRF and 9 for AFM. (8)*

4.2.5 Virally induced lysis of *E. coli*

To observe the dynamics of bleb formation, we followed infected *E. coli* cells by using phase-contrast microscopy. We were able to follow the formation of individual bacterial blebs with a time resolution exceeding that of AFM (Fig. 19AB). However, due to spatial resolution limitations, only large blebs could be observed. The phase-contrast recordings showed the formation of expanding bacterial blebs at various sites of the bacterial surface on a timescale of a few minutes. Blebs were an order of magnitude larger than those identified by AFM. A possible explanation is that AFM images only revealed blebs at the beginning of their formation. If SyO, a membrane impermeable nucleic acid dye used for dead cell staining, is added to the sample, then lysis is immediately followed by a bright fluorescent explosion (Fig. 19C).

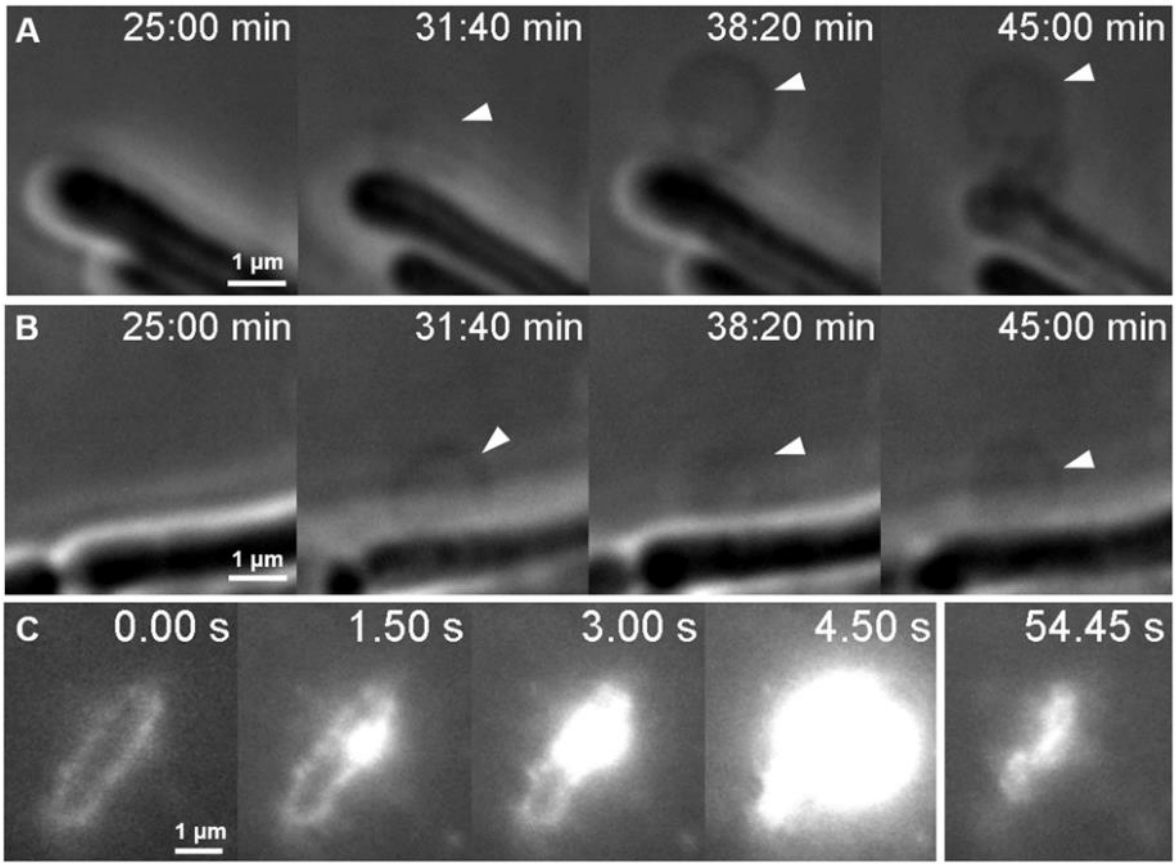

Fig. 19. ***Viral infection induces blebbing and leads to an explosive lysis****.* ***(A)*** *and* ***(B)*** *show two exemplary phase-contrast image series of bacterial blebbing.* ***(C)*** *A TIRF microscopy image series depicting certain moments from the lysis of a single bacterium in the presence of SyO. Timestamp starts from 35 minutes post-infection. (8)*

4.2.6 Photothermally induced DNA release of T7

To investigate the DNA ejection by T7 bacteriophages *in vitro,* we investigated single phage particles immobilized in a microfluidic device and monitored the appearance of DNA by SyO labeling using TIRF microscopy.

In the beginning of the experiment the field of view was dark, and bright spots corresponding to single T7 virions started to appear with a lag time due to *in situ* labeling with SyO (Fig. 20A). After an average lag time of 21 ± 12 s (n = 34) viral DNA was ejected into the medium, where it was immediately stretched out in parallel to the flow direction. DNA ejection was a rapid process, and more than half of the genome was ejected within a fraction of a second (0.13 ± 0.07 s). Remarkably, DNA ejection was

DOI:10.14753/SE.2023.2799

never complete on the experimental time scale, and most of the viral genome (84 ± 5%; n = 134) remained attached to the capsid throughout the observation period (Fig. 20B). 82 % of DNA ejections halted after 80 % of the genome has been released.

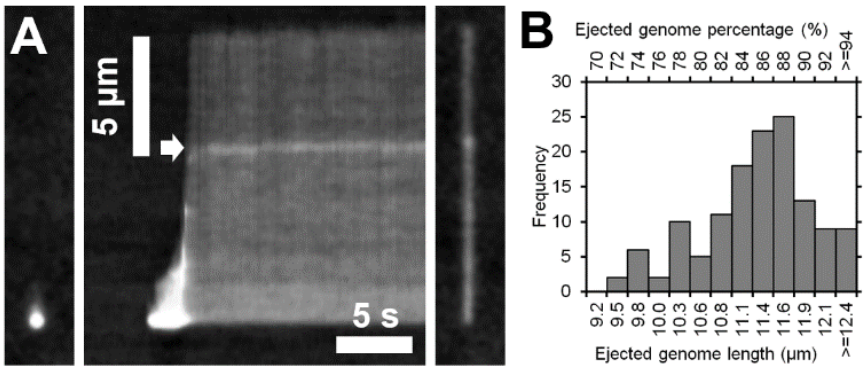

Fig. 20. Bacteriophage DNA ejection in solution. ***(A)*** *Images (left and right), and kymograph (middle) of a bacteriophage ejecting its DNA.* ***(B)*** *Distribution of ejected genome fractions. White arrow points to a more intensely labeled region of DNA. (8)*

Kymographs of DNA ejections often revealed a segment of DNA with a higher fluorescence (Fig. 20A, white arrow). This region was found at one third of the genome measured from the starting end (which was first released), which confirms that DNA release is unidirectional. To investigate whether this more intensely labeled region is related to the presence of proteins or if the DNA contains overlapping regions, we have labeled the amine groups of viral proteins using Alexa-NHS (Fig. 21A). We identified the labeled proteins as the capsid, since this is the part of the phage that is most accessible for the labeling dye.

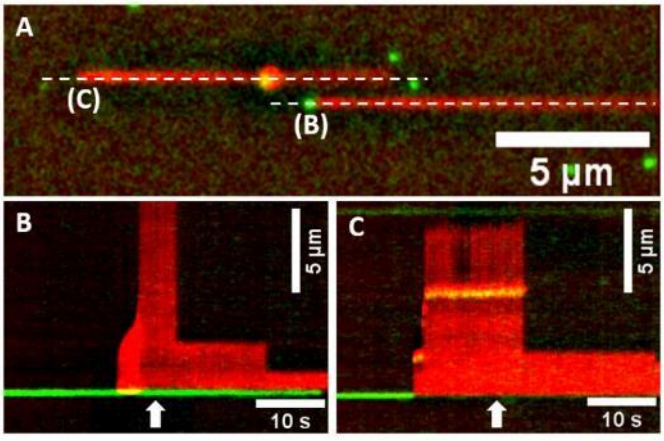

Fig. 21. ***DNA can leak from capsids at two different locations. (A)*** *Fluorescently labeled capsids of T7 (green) release viral DNA in two different manners. White lines and letters in parenthesis show the respective line along which kymographs were created.* ***(B)*** *Kymograph of a phage releasing its DNA in the conventional manner.* ***(C)*** *A phage releasing its DNA in a non-conventional way. White arrows show the moment at which the 2D (A) image was taken.*

In many cases a conventional DNA release was observed, during which the capsid remained bound to the substrate surface, the DNA was continuously ejected from this location, and it remained attached to the capsid (Fig. 21B). However, in many cases a non-conventional ejection was observed (Fig. 21C). Meaning, that similarly to the conventional ejections, the DNA remained attached to the substrate (glass surface), but a major part of the proteins was also released.

5. Discussion

5.1 SARS-CoV-2

5.1.1 SARS-CoV-2 particles are decorated with flexible spike trimers

The height of SARS-CoV-2 particles measured by AFM appeared to be smaller than the diameter measured by cryo-EM (91 ± 11 nm) (15-17). This apparent decrease in height can be attributed to the partial flattening of viral particles as a result of immobilization on the substrate surface. The difference in particle size can also be the result of the state of infected cells. Healthier cells might produce viruses of different size compared to less healthy cultures and *vice versa*. Higher multiplicity of infection could also affect the volume of viruses produced. A higher MOI ratio can result in a higher virus outcome (unless the culture becomes over infected), which can mean that smaller viruses will be produced.

The number of spike trimers per particle measured on AFM images (61) appears to be greater than those measured by cryo-EM (24) (15-17). This difference in the number of spikes can be related to the difference in imaging techniques since AFM is able to measure every single spike that is visible, however some spikes might disappear due to the averaging required in cryo-EM. The difference in number can also result from mutational variants and the difference in viral assembly. Cryo-EM data has already suggested the flexibility of the spikes due to the presence of a hinge region in the spike structure (15-17). Translational motion and rotation of the spikes can arise from their lateral diffusion inside the viral envelope, and also from their internal flexibility at the hinge region. By comparison, and supporting our theory, the surface of native viruses appeared blurry, and their spikes could not be resolved, which we believe to be the result of rapid spike motion. If this motion is faster than the scanning speed of the AFM, then it leads to the apparent smoothing of the viral surface. Considering that the typical pixel sampling frequency (f_s) in these images was 308 Hz, the frequency of spike dynamics exceeds the Nyquist frequency of $f_s/2$ (154 Hz). Because the pixel size (d) is 2 nm, the spikes dynamically fluctuate, within a space limited by their flexible neck, with a speed ($v=df_s/2$) exceeding ~0.3 nm/ms. Most plausibly, spike motion is dictated by the Brownian dynamics of the receptor-binding-domain (RBD) trimer which may then be thought of as a tethered particle. Spike mobility in the virus envelope may contribute further to the observed dynamics. An alternative explanation for the observed blurred virion surface is that the

spikes evade the moving AFM cantilever tip which then scans the envelope surface. We exclude this possibility, however, because, while it relies on a similarly dynamic spike behavior, a reduced virion height should have been observed. We speculate that the rapid spike motion revealed by these experiments contributes to an efficient dynamic search by the virion on the surface of the targeted host cell, which explains why SARS-CoV-2 is at least as infective as the influenza virus (40) in spite of its fewer spikes (up to ~60 in SARS-CoV-2 *versus* up to ~350 in influenza A (41)).

5.1.2 SARS-CoV-2 viruses are mechanically stable and resilient

The stiffness of SARS-CoV-2 virions (13 ± 5 pN/nm) makes them one of the most compliant among many viruses (42, 43). The stiffness of SARS-CoV-2 is an order of magnitude lower than that of the T7 capsid (730 pN/nm) and somewhat lower than the envelope of influenza viruses (20 ± 3 pN/nm) (5, 44). This suggests that the elasticity of SARS-CoV-2 is dominated by its envelope, and the RNP contributes little to the overall viral mechanics. Compared to other viruses, following the yield point of the particle force did not drop to zero, meaning that total collapse was never achieved despite the drastic mechanical perturbation. We hypothesize that the yield of the particle is caused by the dynamic rearrangement of the RNPs inside the particle (17). The repeatability of the indentation cycles could in principle be explained by two alternate mechanisms. The first one is the force-induced virion rolling on the substrate. We exclude this possibility, because, due to the presence of anti-spike-protein antibodies on the surrounding surface, the rolling process is expected to be irreversible. Furthermore, the result of rolling would also be visible in topographical images. The second is the repeated sideways slippage of the cantilever tip, off the virion surface. We exclude this possibility as well based on a calibration of the cantilever's lateral torsion and because this process is expected to be completely reversible. We can only speculate about the mechanisms behind the persistent structural self-healing of SARS-CoV-2. Conceivably, the process involves the dynamic interaction between the RNA, protein, and lipid components. The pulling curves which contained protein unfolding events can be explained by the mechanically-driven unfolding of S protein domains (45). Considering the force response data, we conclude that the mechanical stability and resilience of SARS-CoV-2 appears to be extraordinary

even amongst different viruses, which might provide a possible explanation to its high contagiousness.

5.1.3 SARS-CoV-2 remains structurally intact at high temperatures

SARS-CoV-2 virions display an unexpected global thermal stability, which is likely related to their aerosol and surface stabilities (46). However, the conformational response of the spike proteins as well as their dissociation from the viral surface observed here eventually leads to the heat-induced inactivation of SARS-CoV-2.

5.2 T7 bacteriophage

5.2.1 Possible mechanisms of host cell surface exploration by T7

We suggest two possible mechanisms to explain T7's diffusive target search. First, viral binding to the host cell is a dynamic process during which the fibers repeatedly bind to and unbind from the bacterial surface, thereby allowing the phage to search for a final binding site. The process thus resembles two-dimensional *walking*, requiring at least two surface-bound fibers. In such a process the number of fibers interacting with the surface progressively increases until a stable surface attachment is achieved. Second, and more likely, bacteriophages carry out an initial *rolling* on the bacterial surface until the tail binds to its receptor. Then the fibers are released from their original, capsid-attached arrangement and bind to the bacterial surface to stabilize the T7 capsid in a position optimal for genome ejection and delivery. We note that while both mechanisms require a dynamic surface adhesion during target search, they predict different time-evolution of speed: during *walking* the speed progressively drops; by contrast, during *rolling* it stays constant. A two-dimensional walking mechanism has been proposed before for T7 on theoretical grounds but with no direct experimental evidence (25). In this model the fibers play a key role in the initial anchoring of T7. However, if the number of surface-bound fibers increased with time, then the exploration process should be progressively decelerating (even if we suppose that fiber binding is reversible), which is in contrast to our experimental finding (Fig. 15D). In our alternative model, T7 phages roll on the surface with an essentially constant speed until the tail binds to its receptor. We propose that once the tail is bound, the fibers are released from the side of the capsid and assist in the final positioning and anchoring of the phage to the host. The predicted constant speed

is well supported by our experimental results (Fig. 15D). In this mechanism the fibers play an important role not so much in the target search but in the proper capsid positioning and orientation, so that genome transfer can be faithfully executed. Indeed, fibers are essential for successful infection, as fiberless mutants are non-infective (47). Our model thus presents a novel sequence of binding actions in the viral target search mechanism, proposing that fibers are secondary receptors responsible for stabilization and precise capsid orientation.

5.2.2 DNA release and translocation

The viral delivery of fluorescently labeled DNA into the target cell has been investigated before and shown to result in an increased overall intracellular fluorescence intensity (29). By contrast, we could not measure a noticeable intensity increase inside the infected cells (29). The lack of intracellular fluorescence intensity increment may be explained by the dispersion of the injected DNA in the host cell, hence its escape from the shallow excitation field (roughly 7% of the total volume of an 800-nm-high bacterium is imaged in TIRF). Alternatively, the intercalated DNA might not pass through the narrow channel formed by the elongated tail of the bacteriophage, and the dye molecules are forced to dissociate. The disappearance of fluorescence can also be described by the presence of DNA-dependent polymerases inside the host cell, which would knock off the intercalators while unwinding the DNA double helix. In contrast to lambda phage DNA translocation (1-20 min), T7 was much quicker and more efficient (90% drop in integrated fluorescence intensity in 1 minute). Such accelerated DNA translocation might be explained by a higher pressure inside the T7 capsid (60 atmospheres) compared to lambda (15-20 atmospheres) (48, 49). A major difference between these two types of phages is that lambda has a long tail without any internal proteins, whereas T7 has a short tail and internal core proteins, which might play a crucial role in further accelerating DNA translocation across the bacterial membrane (25). At later stages of infection (30-40 min), phages were still binding to target bacteria; however, no decrease in fluorescence intensity was apparent, indicating that DNA translocation became inhibited by then. Since at this stage all bacteria are expected to be successfully infected by at least one phage, their internal enzymatic machinery has already been drastically reprogrammed and further enzymatically driven DNA translocation might be inhibited.

5.2.3 T7 phages might be knocked off by the AFM tip

Often, phages detected in an AFM image were no longer present at the same location in the subsequent AFM scan. This finding substantiates the notion that T7 phage particles carry out a surface exploration that results in changing position. Alternatively, the AFM scanning may have mechanically knocked off some of the T7 particles that were weakly bound. This explanation predicts that AFM scanning functions as a mechanical disinfectant that slows down the infection cycle. In support of this idea, we observed that most of the bacteria outside the scanning area lysed during the measurements, yet the bacterium that was being scanned did not lyse during a one-hour-long experiment.

5.2.4 Infection by T7 leads to bleb formation and a violent lysis

The explanation of differently sized blebs in phase-contrast and AFM images might be that AFM images only revealed blebs at the start of their formation. The appearance of the blebs is not unique to infection by T7 but can appear as a result of different external factors. One of these effects is the addition of antimicrobial peptides, which can initiate hole formation in the cell wall or the outer membrane (50, 51). The morphology of blebs induced by the addition of antibiotics is similar to the ones appearing as a result of viral infection. These antibiotics can lyse bacteria by forming a pore in the cell wall, which leads to membrane bulging and thereby lysis of the cell (51). Infection by T7 leads to a similar outcome, but the course of actions is somewhat different and bleb formation is not mandatory for lysis. In the case of T7, viral genes encode lysis proteins which act sequentially (32, 52). The first step is pore formation in the inner membrane, which leads to the release of peptidoglycan-digesting enzymes. At this stage the membrane structure is expected to be similar to that proposed by *Wong et al* (51). The peptidoglycan structure becomes sporadically disrupted, which leads to membrane bulging at the defect points. The so formed blebs become weak points where local membrane rupture is more likely to happen, which would finally lead to cell lysis. An open question regarding bleb formation is whether their appearance is a deterministic step in the infection cycle of T7 or a bacterial defensive response mechanism. Viral infection-induced blebbing has already been observed by other groups using fluorescent labeling techniques (33). This immediate increase in fluorescence in SyO containing sample is due to the instantaneous

labeling of freshly released phage progeny. Fluorescence increase after bacterial lysis could also be the result of labeling the bacterial genome, however this is unlikely as infection by T7 leads to host DNA degradation, which allows the efficient replication of the viral genome (53). After about a minute, freshly released phages diffuse away from the dead host to seek further targets viable for infection.

5.2.5 Genome ejection is a virally regulated process

We hypothesize that the mechanism of activation is related to the local heating of the capsid through the absorbance of incorporated DNA-intercalating dye which penetrated the capsid. The observed DNA ejection corresponds to “misfiring” since it started without the presence of the viral receptor. DNA ejection was often halted at the terminal regions of the genome. Lysis-related genes (spanin, holin) are transcribed starting from 91 % of the viral genome (location of first lysis gene, type II holin: 36344/39936 bp, corresponds to 91%) (54). Presumably, the terminal region of the genome carries innate signals that hinder the release of the last segment, thereby delaying the transcription of lysis-related genes. How this mechanical barrier is overcome is still unclear. Regardless of the molecular mechanism, our finding reveals the presence of a mechanical control that tunes the timing of the host cell lysis hence the infection cycle.

5.2.6 Photodamage can lead to capsids breakage

Intercalator excitation can lead to the formation of reactive oxygen species which can damage the capsid as well as the viral genome. DNA breakage can be observed directly since segments of the genome often float away if the covalent bonds of the deoxyribose-phosphate backbone break at two opposing locations (Fig. 21BC). We hypothesize that such photodamaging effects can rupture the wall of the capsid, leading to multiple DNA leakage points, which would explain why the capsid is often found floating along the genome. In this case the end of the genome would be the anchored to the substrate surface. An alternative explanation would be that the tail complex separates from the capsid, and it can either be found sliding along the DNA or it can remain attached to the surface thereby anchoring the genome-capsid complex.

6. Conclusions

The atomic force microscopic imaging and nanomechanical measurements revealed that the SARS-CoV-2 virion is spherical, highly dynamic, compliant, and resilient, and it displays remarkable mechanical and global thermal stabilities. Unfixed, native state measurements revealed a blurred viral surface, which we attribute to rapid spike movements. While the dynamics of the surface spikes may play an important role in the unusually high infectivity of the virus, its mechanical and self-healing properties may also ensure adaptation to a wide range of environmental circumstances. Although SARS-CoV-2 particles are resilient in case of sharp tip indentation, plateau tip compression induces irreversible structural changes.

Viral infection comprises a highly complex series of interconnected and synchronized events. T7 binds reversibly to the *E. coli* surface which it explores for the proper binding site by diffusive motion. It has been postulated that lipopolysaccharide (LPS) is a primary receptor for T7, however we could not confirm these results. By employing TIRF and AFM the docking process of single T7 phages can be observed. Our results suggest that the exploratory motion of T7 entails the rolling of the phage on the bacterial surface rather than walking with the fibers. Phage docking is initiated by binding of the tail to its receptor, and the fibers are involved in capsid positioning for rapid (~1 min) and efficient genome transfer. DNA release can be triggered *in vitro* by a photothermal mechanism which leads to partial genome ejection that stops short of the lysis-related genes, pointing at the presence of a mechanical genome-transfer control. At high excitation levels bleaching derived reactive oxygen species can possibly damage the capsid structure and cause the viral DNA to leak out from multiple points. The T7 infection ends with a violent cell lysis preceded by bacterial membrane surface roughening and bleb formation. Single virus observations such as the ones employed in this work can greatly contribute to the general understanding of nature's nanomachines.

Novel, thesis-related findings:

1) Native SARS-CoV-2 particles display a blurred surface as observed by AFM, which is related to rapid spike movements.

2) SARS-CoV-2 is highly resilient mechanically and can recover from multiple sharp tip indentation cycles. SARS-CoV-2 is among the most elastic viral nanoparticles.
3) The global structure of SARS-CoV-2 remains unchanged during heating cycles up to 90°C, however spikes dissociate from the viral surface.
4) T7 bacteriophages bind to their target cells in a reversible manner.
5) We suggest that target bound bacteriophages are not “walking” but exploring the host cell surface by a non-specific adhesion mediated rolling process.
6) DNA injection is a rapid (1 min) process, whereby most of the genome (~90%) is transferred into the target cell.
7) In the presence of certain DNA intercalators T7 genome ejection can be photothermally triggered by high laser excitation levels.
8) Photothermally triggered DNA release is incomplete, 80% of DNA ejections halt after ejecting ~82% of the genome.

DOI:10.14753/SE.2023.2799

7. **Summary**

In my thesis I focus on the nanomechanics and infection processes of viruses. I have studied two different types of viruses: the recently emerged SARS-CoV-2 and the T7 bacteriophage which is one of the workhorses of virus research. Although similar in size, the two viruses, have very different structure and infection mechanisms.

SARS-CoV-2 is an enveloped ssRNA virus, which uses its spike proteins to attach and invade the host via membrane fusion. We have imaged individual virions employing AFM and found that their surface is covered by ~ 61 spikes per virus. Imaging native, unfixed viruses has revealed that the spikes are highly flexible, which might play an important role in target recognition. SARS-CoV-2 particles are highly elastic and following sharp tip indentation their initial shape is restored. Comparatively, plateau tip compression results in irreversible structural changes, whereby the virion collapses. Upon heating, spikes are progressively released from the virions surface, yet their global morphology stays the same.

T7 bacteriophages are dsDNA viruses, which infect *E. coli* with high efficiency. Their structure consists of a protein capsid, filled with viral DNA and internal core proteins, connected to a tail-fiber complex. By employing fluorescent labeling, we have found that host recognition of T7 phages is a rather dynamic process, whereby the virus explores the bacterial surface, presumably by a rolling mechanism. AFM imaging revealed stably anchored bacteriophages, achieved by tail-fiber complex to host receptor binding. The six anchored fibers of a given T7 phage displayed isotropic spatial orientation. Successful receptor recognition leads to viral genome translocation. We have found that in case of DNA labeled phages, ejection can be photothermally triggered. *In vitro* DNA ejection experiments have shown that genome release abruptly halts at the terminal 10% of the genome. We hypothesize that withholding this terminal region has a regulatory function during infection, namely that lysis related genes are reserved until a host lysis is required. The exact mechanism which signals the phage to release this terminal region is not yet understood. In the final phase of infection virally induced bleb formation was observed, finally leading to host cell lysis and the release of phage progeny.

8. References

1. Piret J, Boivin G. (2021) Pandemics throughout history. Frontiers in Microbiology, 11: 631736.
2. Zhou P, Yang XL, Wang XG, Hu B, Zhang L, Zhang W, Si HR, Zhu Y, Li B, Huang CL, Chen HD, Chen J, Luo Y, Guo H, Jiang RD, Liu MQ, Chen Y, Shen XR, Wang X, Zheng XS, Zhao K, Chen QJ, Deng F, Liu LL, Yan B, Zhan FX, Wang YY, Xiao GF, Shi ZL. (2020) A pneumonia outbreak associated with a new coronavirus of probable bat origin. Nature, 579: 270-273.
3. Zhu N, Zhang D, Wang W, Li X, Yang B, Song J, Zhao X, Huang B, Shi W, Lu R, Niu P, Zhan F, Ma X, Wang D, Xu W, Wu G, Gao GF, Tan W, China Novel Coronavirus I, Research T. (2020) A Novel Coronavirus from Patients with Pneumonia in China, 2019. N Engl J Med, 382: 727-733.
4. Voros Z, Csik G, Herenyi L, Kellermayer M. (2018) Temperature-Dependent Nanomechanics and Topography of Bacteriophage T7. J Virol, 92.
5. Vörös Z, Csík G, Herényi L, Kellermayer MSZ. (2017) Stepwise reversible nanomechanical buckling in a viral capsid. Nanoscale, 9: 1136-1143.
6. Tóth K, Csik G, Rontó GY. (1987) Salt effects on the bacteriophage T7-II structure and activity changes. Physiological chemistry and physics and medical NMR, 19: 67-74.
7. Gábor F, Szolnoki J, Tóth K, Fekete A, Maillard P, Csík G. (2001) Photoinduced Inactivation of T7 Phage Sensitized by Symmetrically and Asymmetrically Substituted Tetraphenyl Porphyrin: Comparison of Efficiency and Mechanism of Action¶. Photochemistry and Photobiology, 73: 304-311.
8. Kiss B, Kiss LA, Lohinai ZD, Mudra D, Tordai H, Herenyi L, Csík G, Kellermayer M. (2022) Imaging the Infection Cycle of T7 at the Single Virion Level. International Journal of Molecular Sciences, 23.
9. Kiss B, Kis Z, Pályi B, Kellermayer MSZ. (2021) Topography, Spike Dynamics, and Nanomechanics of Individual Native SARS-CoV-2 Virions. Nano Letters, 21: 2675-2680.
10. Hoffmann M, Kleine-Weber H, Schroeder S, Kruger N, Herrler T, Erichsen S, Schiergens TS, Herrler G, Wu NH, Nitsche A, Muller MA, Drosten C, Pohlmann

S. (2020) SARS-CoV-2 Cell Entry Depends on ACE2 and TMPRSS2 and Is Blocked by a Clinically Proven Protease Inhibitor. Cell, 181: 271-280 e278.

11. Walls AC, Park YJ, Tortorici MA, Wall A, McGuire AT, Veesler D. (2020) Structure, Function, and Antigenicity of the SARS-CoV-2 Spike Glycoprotein. Cell, 181: 281-292 e286.
12. Henderson R, Edwards RJ, Mansouri K, Janowska K, Stalls V, Gobeil SMC, Kopp M, Li D, Parks R, Hsu AL, Borgnia MJ, Haynes BF, Acharya P. (2020) Controlling the SARS-CoV-2 spike glycoprotein conformation. Nat Struct Mol Biol, doi:10.1038/s41594-020-0479-4.
13. McCallum M, Walls AC, Bowen JE, Corti D, Veesler D. (2020) Structure-guided covalent stabilization of coronavirus spike glycoprotein trimers in the closed conformation. Nat Struct Mol Biol, doi:10.1038/s41594-020-0483-8.
14. Wrapp D, Wang N, Corbett KS, Goldsmith JA, Hsieh CL, Abiona O, Graham BS, McLellan JS. (2020) Cryo-EM structure of the 2019-nCoV spike in the prefusion conformation. Science, 367: 1260-1263.
15. Ke Z, Oton J, Qu K, Cortese M, Zila V, McKeane L, Nakane T, Zivanov J, Neufeldt CJ, Cerikan B, Lu JM, Peukes J, Xiong X, Krausslich HG, Scheres SHW, Bartenschlager R, Briggs JAG. (2020) Structures and distributions of SARS-CoV-2 spike proteins on intact virions. Nature, doi:10.1038/s41586-020-2665-2.
16. Turonova B, Sikora M, Schurmann C, Hagen WJH, Welsch S, Blanc FEC, von Bulow S, Gecht M, Bagola K, Horner C, van Zandbergen G, Landry J, de Azevedo NTD, Mosalaganti S, Schwarz A, Covino R, Muhlebach MD, Hummer G, Krijnse Locker J, Beck M. (2020) In situ structural analysis of SARS-CoV-2 spike reveals flexibility mediated by three hinges. Science, doi:10.1126/science.abd5223.
17. Yao H, Song Y, Chen Y, Wu N, Xu J, Sun C, Zhang J, Weng T, Zhang Z, Wu Z, Cheng L, Shi D, Lu X, Lei J, Crispin M, Shi Y, Li L, Li S. (2020) Molecular architecture of the SARS-CoV-2 virus. Cell, doi:10.1016/j.cell.2020.09.018.
18. Santos IdA, Grosche VR, Bergamini FRG, Sabino-Silva R, Jardim ACG. (2020) Antivirals Against Coronaviruses: Candidate Drugs for SARS-CoV-2 Treatment? Frontiers in Microbiology, 11.

19. Hulo C, de Castro E, Masson P, Bougueleret L, Bairoch A, Xenarios I, Le Mercier P. (2011) ViralZone: a knowledge resource to understand virus diversity. Nucleic Acids Research, 39: D576-D582.
20. Cuervo A, Fàbrega-Ferrer M, Machón C, Conesa JJ, Fernández FJ, Pérez-Luque R, Pérez-Ruiz M, Pous J, Vega MC, Carrascosa JL. (2019) Structures of T7 bacteriophage portal and tail suggest a viral DNA retention and ejection mechanism. Nature Communications, 10: 1-11.
21. Vörös Z, Csík G, Herényi L, Kellermayer M. (2018) Temperature-dependent nanomechanics and topography of bacteriophage T7. Journal of Virology, 92: e01236-01218.
22. Kellermayer MSZ, Voros Z, Csik G, Herenyi L. (2018) Forced phage uncorking: viral DNA ejection triggered by a mechanically sensitive switch. Nanoscale, 10: 1898-1904.
23. Kemp P, Gupta M, Molineux IJ. (2004) Bacteriophage T7 DNA ejection into cells is initiated by an enzyme-like mechanism. Molecular Microbiology, 53: 1251-1265.
24. Molineux IJ, Panja D. (2013) Popping the cork: mechanisms of phage genome ejection. Nature Reviews Microbiology, 11: 194.
25. Hu B, Margolin W, Molineux IJ, Liu J. (2013) The Bacteriophage T7 Virion Undergoes Extensive Structural Remodeling During Infection. Science, 339: 576-579.
26. Molineux IJ. (2001) No syringes please, ejection of phage T7 DNA from the virion is enzyme driven. Molecular Microbiology, 40: 1-8.
27. Mangenot S, Hochrein M, Rädler J, Letellier L. (2005) Real-Time Imaging of DNA Ejection from Single Phage Particles. Current Biology, 15: 430-435.
28. Grayson P, Han L, Winther T, Phillips R. (2007) Real-time observations of single bacteriophage λ DNA ejections in vitro. Proceedings of the National Academy of Sciences, 104: 14652.
29. Van Valen D, Wu D, Chen Y-J, Tuson H, Wiggins P, Phillips R. (2012) A Single-Molecule Hershey-Chase Experiment. Current Biology, 22: 1339-1343.

30. Smith DE, Tans SJ, Smith SB, Grimes S, Anderson DL, Bustamante C. (2001) The bacteriophage φ29 portal motor can package DNA against a large internal force. Nature, 413: 748.
31. Young R. (2014) Phage lysis: Three steps, three choices, one outcome. Journal of Microbiology, 52: 243-258.
32. Summer EJ, Berry J, Tran TAT, Niu L, Struck DK, Young R. (2007) Rz/Rz1 Lysis Gene Equivalents in Phages of Gram-negative Hosts. Journal of Molecular Biology, 373: 1098-1112.
33. Mandal PK, Ballerin G, Nolan LM, Petty NK, Whitchurch CB. (2021) Bacteriophage infection of Escherichia coli leads to the formation of membrane vesicles via both explosive cell lysis and membrane blebbing. Microbiology, 167.
34. de Pablo PJ, Schaap IAT. (2019) Atomic Force Microscopy of Viruses. Adv Exp Med Biol, 1215: 159-179.
35. Kiss B, Mudra D, Torok G, Martonfalvi Z, Csik G, Herenyi L, Kellermayer M. (2020) Single-particle virology. Biophys Rev, doi:10.1007/s12551-020-00747-9.
36. Zupán K, Egyeki M, Toth K, Fekete A, Herényi L, Módos K, Csík G. (2008) Comparison of the efficiency and the specificity of DNA-bound and free cationic porphyrin in photodynamic virus inactivation. Journal of Photochemistry and Photobiology B: Biology, 90: 105-112.
37. Biebricher AS, Heller I, Roijmans RFH, Hoekstra TP, Peterman EJG, Wuite GJL. (2015) The impact of DNA intercalators on DNA and DNA-processing enzymes elucidated through force-dependent binding kinetics. Nature Communications, 6: 7304.
38. Tinevez J-Y, Perry N, Schindelin J, Hoopes GM, Reynolds GD, Laplantine E, Bednarek SY, Shorte SL, Eliceiri KW. (2017) TrackMate: An open and extensible platform for single-particle tracking. Methods, 115: 80-90.
39. Shabram P, Aguilar-Cordova E. (2000) Multiplicity of infection/multiplicity of confusion. Molecular Therapy, 2: 420-421.
40. Petersen E, Koopmans M, Go U, Hamer DH, Petrosillo N, Castelli F, Storgaard M, Al Khalili S, Simonsen L. (2020) Comparing SARS-CoV-2 with SARS-CoV and influenza pandemics. The Lancet Infectious Diseases, 20: e238-e244.

41. Harris A, Cardone G, Winkler DC, Heymann JB, Brecher M, White JM, Steven AC. (2006) Influenza virus pleiomorphy characterized by cryoelectron tomography. Proc Natl Acad Sci U S A, 103: 19123-19127.
42. Cieplak M, Robbins MO. (2013) Nanoindentation of 35 virus capsids in a molecular model: relating mechanical properties to structure. PLoS One, 8: e63640.
43. Mateu MG. (2012) Mechanical properties of viruses analyzed by atomic force microscopy: a virological perspective. Virus Res, 168: 1-22.
44. Li S, Eghiaian F, Sieben C, Herrmann A, Schaap IAT. (2011) Bending and puncturing the influenza lipid envelope. Biophys J, 100: 637-645.
45. Moreira RA, Chwastyk M, Baker JL, Guzman HV, Poma AB. (2020) Quantitative determination of mechanical stability in the novel coronavirus spike protein. Nanoscale, 12: 16409-16413.
46. van Doremalen N, Bushmaker T, Morris DH, Holbrook MG, Gamble A, Williamson BN, Tamin A, Harcourt JL, Thornburg NJ, Gerber SI, Lloyd-Smith JO, de Wit E, Munster VJ. (2020) Aerosol and Surface Stability of SARS-CoV-2 as Compared with SARS-CoV-1. N Engl J Med, 382: 1564-1567.
47. Kemp P, Garcia LR, Molineux IJ. (2005) Changes in bacteriophage T7 virion structure at the initiation of infection. Virology, 340: 307-317.
48. Ivanovska I, Wuite G, Jönsson B, Evilevitch A. (2007) Internal DNA pressure modifies stability of WT phage. Proceedings of the National Academy of Sciences, 104: 9603.
49. Chang C-Y, Kemp P, Molineux IJ. (2010) Gp15 and gp16 cooperate in translocating bacteriophage T7 DNA into the infected cell. Virology, 398: 176-186.
50. MacDonald IA, Kuehn MJ. (2012) Offense and defense: microbial membrane vesicles play both ways. Research in Microbiology, 163: 607-618.
51. Wong F, Amir A. (2019) Mechanics and Dynamics of Bacterial Cell Lysis. Biophysical Journal, 116: 2378-2389.
52. Young R. (1992) Bacteriophage lysis: mechanism and regulation. Microbiological Reviews, 56: 430-481.

53. Center MS, Studier FW, Richardson CC. (1970) The structural gene for a T7 endonuclease essential for phage DNA synthesis. Proceedings of the National Academy of Sciences of the United States of America, 65: 242-248.

54. Dunn JJ, Studier FW, Gottesman M. (1983) Complete nucleotide sequence of bacteriophage T7 DNA and the locations of T7 genetic elements. Journal of Molecular Biology, 166: 477-535.

9. Bibliography

Publications related to the thesis

1. Kiss, B., Kis, Z., Pályi, B., & Kellermayer, M. S. (2021). Topography, spike dynamics, and nanomechanics of individual native SARS-CoV-2 virions. Nano letters, 21(6), 2675-2680.
2. Kiss, B., Kiss, L. A., Lohinai, Z. D., Mudra, D., Tordai, H., Herenyi, L., ... & Kellermayer, M. (2022). Imaging the Infection Cycle of T7 at the Single Virion Level. International Journal of Molecular Sciences, 23(19), 11252.

Unrelated publications

Research Articles

1. Padányi, R., Farkas, B., Tordai, H., Kiss, B., Grubmüller, H., Soya, N., ... & Hegedűs, T. (2022). Nanomechanics combined with HDX reveals allosteric drug binding sites of CFTR NBD1. Computational and Structural Biotechnology Journal.
2. Kellermayer, D., Kiss, B., Tordai, H., Oláh, A., Granzier, H. L., Merkely, B., ... & Radovits, T. (2021). Increased expression of N2BA titin corresponds to more compliant myofibrils in athlete's heart. International journal of molecular sciences, 22(20), 11110.
3. Kiss, B., Bozó, T., Mudra, D., Tordai, H., Herényi, L., & Kellermayer, M. (2021). Development, structure and mechanics of a synthetic E. coli outer membrane model. Nanoscale Advances, 3(3), 755-766.
4. Máthé, D., Kiss, B., Pályi, B., Kis, Z., Forgách, L., Hegedűs, N., ... & Kellermayer, M. S. (2021). The 3M Concept: Biomedical Translational Imaging from Molecules to Mouse to Man. The EuroBiotech Journal, 5(3), 155-160.
5. Forgách, L., Hegedűs, N., Horváth, I., Kiss, B., Kovács, N., Varga, Z., ... & Máthé, D. (2020). Fluorescent, Prussian Blue-Based Biocompatible Nanoparticle System for Multimodal Imaging Contrast. Nanomaterials, 10(9), 1732.
6. Kiss, B., Mudra, D., Török, G., Mártonfalvi, Z., Csík, G., Herényi, L., & Kellermayer, M. (2020). Single-particle virology. Biophysical Reviews, 12(5), 1141-1154..

7. Kretzer, B., Kiss, B., Tordai, H., Csík, G., Herényi, L., & Kellermayer, M. (2020). Single-Molecule Mechanics in Ligand Concentration Gradient. Micromachines, 11(2), 212..
8. Hegedűs, N., Forgách, L., Kiss, B., Varga, Z., Jezsó, B., Horváth, I., ... & Máthé, D. (2022). Synthesis and preclinical application of a Prussian blue-based dual fluorescent and magnetic contrast agent (CA). PloS one, 17(7), e0264554.

DOI:10.14753/SE.2023.2799

10. **Acknowledgements**

First of all, I want to express my gratitude to my supervisor: Miklós Kellermayer who has invited me as a graduate student to start research in his lab. From the moment we started to work together he has treated me as his equal in science, which was the most unusual welcome from a professor at his level. He has always been very kind and supportive throughout my PhD; he stayed open to my research ideas even to those which felt extremely challenging. Most important above all, he has taught me the "scientific way" of thinking and writing. I am grateful for getting to know Levente Herényi who was always curious about my new results, even if they meant failed experiments, day after day. I had some of the most interesting scientific discussions with him, apart from which he also taught me valuable life lessons. I would like to thank Hedvig Tordai for her unbreakable patience towards me, since she was the one who was most frequently bombarded with my questions. I have learned nearly all molecular biological techniques from her, which laid the foundations for successful single-molecule and single-particle experiments. I would also like to thank Tamás Bozó, who taught me the basics of working in a lab, and who was patient enough to teach me "the ways of the AFM". Furthermore, I would like to thank Zoltán Kis, and Bernadett Pályi, who have purified and prepared the SARS-CoV-2 samples for AFM imaging. I am most thankful for the work of Gabriella Csík, who has optimized the isolation and purification of T7 bacteriophages, without such pure samples my work would not have been possible. I continuously appreciated the work of Krisztina Lór, Mónika Komárné Drabbant and Erzsébet Besze. Without them, the lab could not have functioned as flawlessly as it did during my PhD.

Altogether, I feel fortunate, that I can say: I was always looking forward to Mondays, when I could return to the Biophysics Department. It has always been a cheerful and inspiring work environment for this I am thankful to every single member of the department, particularly to my fellow PhD students. I am most grateful for the friendship of Anna Hollósi, my partner in science.

Finally, I am thankful for the support of my family and friends, who have always been understanding with me, even when the long experimental days sometimes overruled the weekend schedules.